nature communications

Article

https://doi.org/10.1038/s41467-025-65568-4

# The neuropathy-linked protein TECPR2 is a Rab5 effector that regulates cargo recycling from early endosomes

Received: 2 October 2024

Accepted: 17 October 2025

**Sankalita Paul**[1], **Rajat Pant**[1], **Poonam Sharma**[1], **Kshitiz Walia**[2,3], **Suhasi Gupta**[4], **Adhil Aseem**[1], **Kamlesh Kumari Bajwa**[1], **Ruben George**[1], **Yudish Varma**[1], **Tripta Bhatia**[4], **Rajesh Ramachandran**[1], **Amit Tuli**[2,3] & **Mahak Sharma**[1]

Small GTP-binding proteins of the Rab, Arf, and Arf-like family mediate the recruitment of their effectors to subcellular membrane-bound compartments, which in turn mediate vesicle budding, motility, and tethering. Here, we report that Tectonin-β-propeller repeat containing protein 2 (TECPR2), a protein mutated in a form of hereditary sensory and autonomic neuropathy (HSAN), is an effector of early endosomal Rab protein, Rab5. We demonstrate that the HSAN-associated missense variants of TECPR2 are defective in Rab5 binding and, consequently, in membrane recruitment. Furthermore, our findings reveal that depletion of TECPR2 impairs recycling of a subset of cargo receptors, including α5β1 integrins, leading to their lysosomal degradation. TECPR2 interacts with SNX17 and subunits of the WASH complex, molecular players that regulate the formation of actin-dependent cargo retrieval subdomain on the early endosomes. Finally, we show that TECPR2 depletion in zebrafish embryos results in decreased survival, impaired movement and altered neuromuscular synaptic morphology. Our study suggests that TECPR2 functions as a linker between Rab5 and the actin-dependent cargo retrieval machinery, providing insights into how mutations in TECPR2 may result in a neurodegenerative disorder.

Vesicular transport consists of several steps, including vesicle budding at the donor membranes, vesicle motility on the microtubule tracks, tethering with the acceptor membranes, and finally membrane fusion. Rabs, Arfs, and Arls (Arf-like) are small GTP-binding (G) proteins of the Ras superfamily that act as master regulators of vesicular transport to and from these membranes. When bound to GTP, small G proteins localize to specific subcellular compartments and recruit effector proteins to these membranes. These effector proteins control different steps of vesicular transport[1].

Rab5 and Rab7 are two key Rab proteins that orchestrate the various steps of early-to-late endosomal transport. Rab5 promotes homotypic fusion and motility of early endosomes and recruits the Rab7 GEF, Mon1-CCZ1, to early endosomes, which in turn mediates Rab7 activation and maturation of early endosomes to late endosomes[2,3]. Early-to-late endosome maturation is coordinated with the retrieval of cargo receptors destined for recycling to the cell surface or towards the trans-Golgi network (TGN) from maturing early endosomes[4,5]. The late endosomal small G protein Rab7 recruits the

---

[1]Department of Biological Sciences, Indian Institute of Science Education and Research Mohali (IISERM), Punjab, India. [2]Academy of Scientific and Innovative Research (AcSIR), Ghaziabad, Uttar Pradesh, India. [3]Division of Cell Biology and Immunology, CSIR-Institute of Microbial Technology (IMTECH), Chandigarh, India. [4]Department of Physical Sciences, Indian Institute of Science Education and Research Mohali (IISERM), Punjab, India. e-mail: msharma@iisermohali.ac.in

microtubule motor dynein-dynactin complex via its effector RILP to mediate retrograde motility of late endosomes towards the perinuclear region[6]. Tethering and fusion of late endosomes with lysosomes is mediated by Rab7 and Arl8b, an Arl family member that localizes to lysosomes. Arl8b interacts with the heterohexameric tethering factor, HOmotypic fusion and Protein Sorting (HOPS) complex, and Rab7 effector PLEKHM1, a multidomain adaptor protein that mediates lysosome fusion with late endosomes and amphisomes[7–9]. Rab2, another Rab protein, interacts with the HOPS complex and regulates tethering and fusion of amphisomes and late endosomes with lysosomes[9,10].

Our ongoing interest in the regulation of membrane fusion machinery on lysosomes led us to a prior study describing the interaction of HOPS complex with a protein known as Tectonin-β-propeller repeat containing protein 2 (TECPR2)[11]. TECPR2 was initially identified as an interacting partner of human autophagy-related 8 (ATG8) family members (LC3 and GABARAPs)[12]. In a subsequent study, a frameshift deletion in *TECPR2* (L1139Rfs*75) was identified in the autosomal-recessive form of an ultra-rare genetic disorder, hereditary sensory and autonomic neuropathy (HSAN) 9 (previously known as spastic paraplegia-49; OMIM 615031)[13]. HSANs are neurodevelopmental and neurodegenerative disorders that can occur due to mutations in multiple genes and are characterized by the progressive loss of autonomic and sensory peripheral nervous system functions.

The N-terminal region (23-343 a.a.) of TECPR2 contains WD40 repeats predicted to fold into a seven-bladed β-propeller fold. The middle region (356-790 a.a.) is intrinsically disordered and lacks any discernible domains, whereas the C-terminal region (945-1353 a.a.) contains six TECPR repeats, which are predicted to form a double β-propeller motif. The last four residues of TECPR2 (WEVI; 1407-1411 a.a.) constitute a conventional W-type LC3-interacting region (LIR) motif that binds LC3 and GABARAP proteins (Fig. 1A). The reported frameshift founder mutations in *TECPR2* (L1139Rfs*75 and L440Rfs*19) lead to the formation of a truncated protein, which is not stable and is degraded in cells[13,14]. To date, several HSAN disease-associated mutations in *TECPR2* have been identified[15], as illustrated in Fig. 1A. The pathogenic mutations in TECPR2 map to conserved residues in the N-terminal WD40 and C-terminal TECPR repeats, indicating that these regions play critical roles in regulating TECPR2 function (Fig. 1A).

Previous studies have shown that TECPR2 regulates the stability of its interaction partners, including HOPS and BLOC-1 complexes and the COPII coat subunits SEC24D-SEC23, although the functional significance of TECPR2 interaction with HOPS and BLOC-1 complexes remains unclear[11]. TECPR2 was reported to localize to membrane fractions containing ER, ERES, and ER-Golgi intermediate compartment (ERGIC) protein markers[14]. TECPR2-depleted cells showed reduced functional ER exit sites (ERES) and delayed secretory cargo export from the ER to the Golgi. Consistent with this, a subsequent study showed that the plasma membrane proteome, secreted proteome, and lysosome composition were also altered upon the loss of TECPR2[11,14]. TECPR2 has also been suggested to play a role in autophagosome biogenesis via LC3C-mediated recruitment to the phagophore membrane, wherein it may regulate membrane export from the ER[11]. However, recent studies have suggested a role for TECPR2 in the later steps of autophagy, i.e., in autophagosome-lysosome fusion. Autophagosome accumulation has been reported in SPG49/HSAN9 patient fibroblasts, and reduced LC3 degradation has been observed in cells lacking TECPR2 expression[16]. In line with this, accumulation of autophagosomes was also observed in a *Tecpr2* knockout mouse model, indicating a defect in autophagosome-lysosome fusion[17].

Our attempts to characterize TECPR2 localization were inconclusive due to the lack of commercially available antibodies that detect the endogenous protein in immunofluorescence assays. Furthermore, consistent with previous findings, overexpression of epitope-tagged full-length TECPR2 showed a mostly cytosolic distribution (Fig. 2A)[11,16]. As small G proteins of the Rab family are key regulators of vesicular transport that mediate recruitment of their downstream effectors on intracellular membranes, we tested whether a Rab protein could serve as an interaction partner for TECPR2 and regulate its membrane recruitment and function.

Here, we report that TECPR2 interacts with early endosomal small G protein Rab5 and localizes to early endosomes in a Rab5-dependent manner. We characterized HSAN-associated TECPR2 mutants and found that a missense mutation, R1336W, disrupts TECPR2 interaction with Rab5, thereby disrupting TECPR2 membrane recruitment. TECPR2-depleted cells failed to efficiently recycle endocytosed α5β1 integrin receptors back to the cell surface, resulting in a reduced number of focal adhesions and, in turn, reduced cell spreading. We found that TECPR2 interacts with Sorting Nexin 17 (SNX17) and the Actin-related protein 2/3 (Arp2/3)-associated actin nucleation-promoting factor (NPF) WASH complex that regulates retrieval of endocytosed α5β1 integrin from lysosomal degradation and mediates their recycling back to the cell surface. TECPR2 depletion led to reduced localization of Arp2/3 complex subunits on early endosomes, and accordingly, actin association with early endosomes was reduced in these cells. We also show that TECPR2 interaction with Rab5 is conserved in zebrafish, and the Rab5-binding defective Tecpr2 mutant is unable to rescue the loss of viability and larval motility defects in Tecpr2 morphants. Thus, TECPR2 is a linker between Rab5 and endosomal sorting adaptors and WASH complex, promoting actin association and formation of membrane subdomains that mediate retrieval of specific cargo receptors from a lysosomal degradation fate.

## Results

### TECPR2 directly binds to Rab5 via its C-terminal TECPR repeats

To test whether any of the Rab proteins could interact with TECPR2, we performed yeast two-hybrid screening of TECPR2 with GTP-locked mutants of the selected candidate Rab proteins. As a positive control, we first confirmed the interaction of TECPR2 with its known binding partners, LC3B and the HOPS complex. As shown in Supplementary Fig. S1A, TECPR2 interacted with LC3B and HOPS subunits Vps41, Vps39, Vps33a, and Vps16, and very weakly with Vps11. Both Vps33a and Vps39 showed self-activation in this assay; however, yeast growth with TECPR2 (WT) was greater than that with the control. For Rab screening, we took 20 of the 70 mammalian Rab proteins in their constitutively active form, which are functionally characterized and available in our laboratory (Fig. 1B). Among these subsets of Rab proteins, Rab5 (Q79L) and Rab29 (Q67L) showed an interaction with TECPR2. Interestingly, previous studies employing high-throughput approaches for protein-protein interactions had identified TECPR2 as a potential interaction partner for Rab5[18,19]. Rab5 is an extensively studied Rab protein; however, its association with TECPR2 was not known through previous studies. Therefore, we pursued the significance of this interaction with Rab5 to gain an understanding of the subcellular function of TECPR2.

We validated that Rab5 binds to TECPR2 in its GTP-bound, but not GDP-bound conformation using constitutively dominant-active and -negative Rab5 point mutants (Q79L and S34N, respectively) in a yeast two-hybrid assay (Fig. 1C). The Rab5 (Q79L) mutant bound to TECPR2 more strongly in a qualitative sense than the wild-type Rab5 (WT), which is consistent with the behavior of other Rab effectors. We also performed co-immunoprecipitation assays that showed GFP-tagged Rab5 interacts with endogenous TECPR2 preferentially in its GTP-bound state, and a significantly reduced interaction was observed with the constitutively GDP-bound Rab5 mutant (Fig. 1D). Finally, using co-immunoprecipitation assays, we confirmed that Rab5 interacts with TECPR2 under endogenous conditions (Fig. 1E).

Next, we investigated the binding region of TECPR2, which is required for its interaction with Rab5. We created TECPR2 mutants either lacking or containing the C-terminal TECPR repeats, i.e., TECPR2

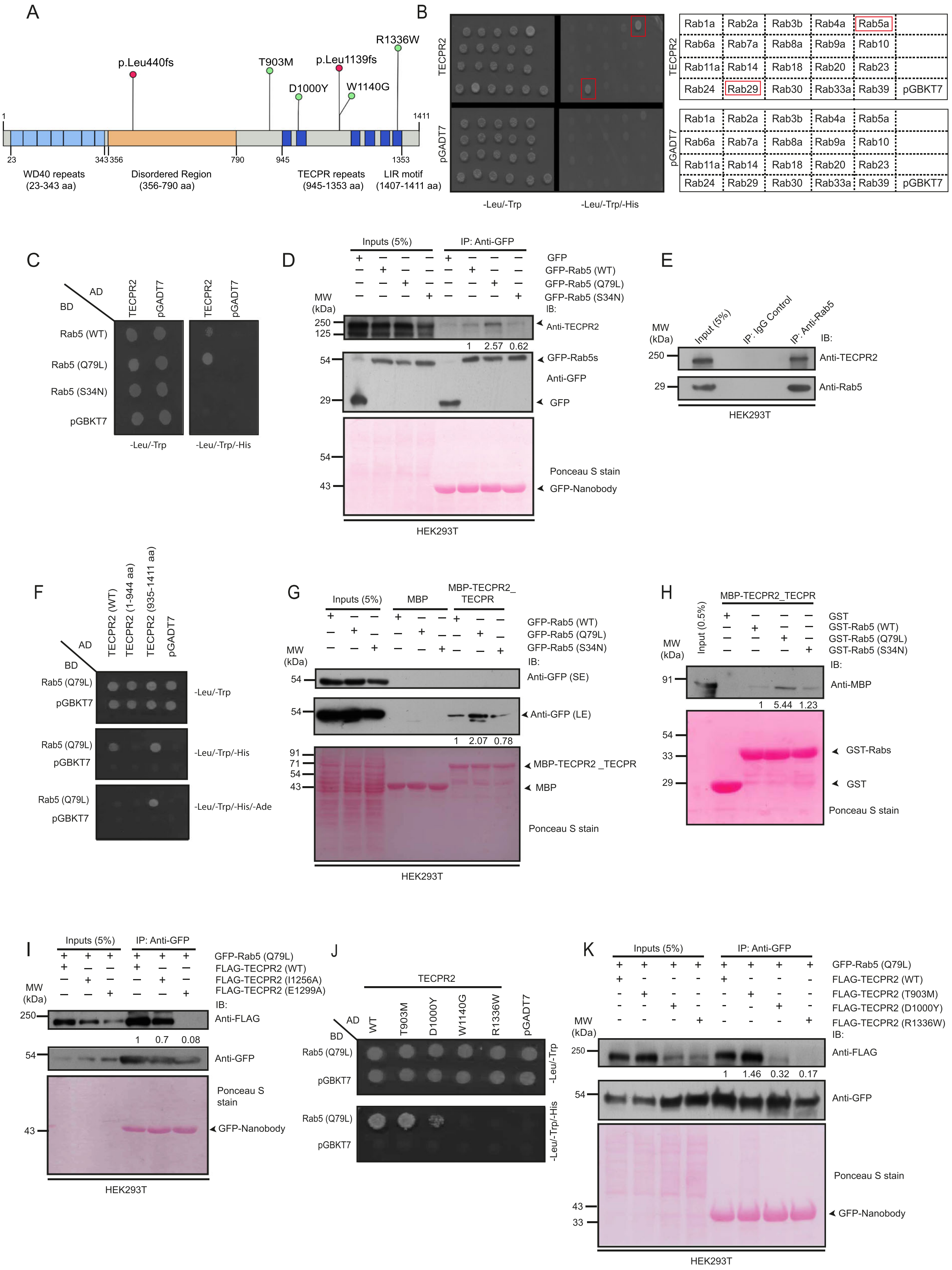

(1-944 a.a.) and TECPR2 (935-1411 a.a.), and tested their ability to interact with Rab5 in a yeast two-hybrid assay. As shown in Fig. 1F, the TECPR2 fragment spanning amino acids 935 to 1411 was both essential and sufficient for binding to Rab5 (Q79L), while no interaction was observed with the TECPR2 fragment spanning amino acids 1 to 944. Notably, Rab5 showed qualitatively greater interaction with the TECPR2 (935-1411 a.a.) fragment than with TECPR2 (WT), suggesting that the N-terminal region of TECPR2 may play an autoinhibitory role in regulating binding to Rab5. Next, we recombinantly expressed and purified MBP-tagged TECPR2 (935-1411 a.a.) (henceforth labeled as TECPR2_TECPR) and incubated the purified protein with cell lysates expressing GFP-tagged WT and constitutively GTP-bound and GDP-bound forms of Rab5. As shown in Fig. 1G, the pulldown assay revealed

**Fig. 1 | TECPR2 directly binds to Rab5 via its C-terminal TECPR repeats.** **A** Domain architecture of TECPR2. Green and red dots indicate the HSAN9-associated variants and TECPR2 founder variants, respectively. **B, C** Yeast two-hybrid assay of TECPR2 with GTP-locked mutants of selected Rab proteins (**B**) and with Rab5 (WT) and mutants (**C**). Co-transformants were spotted on -Leu/-Trp and -Leu/-Trp/-His to confirm viability and detect interactions, respectively. **D** HEK293T cell lysates expressing indicated GFP-tagged proteins were immunoprecipitated with anti-GFP and immunoblotted (IB) with the indicated antibodies. The anti-GFP nanobody was visualized using Ponceau S staining. Densitometric analysis of TECPR2, normalized to the input and direct IP, is shown. **E** HEK293T cell lysates were immunoprecipitated with anti-Rab5 or mouse IgG (used as a control) and IB with indicated antibodies. **F** Yeast two-hybrid assay of TECPR2 (WT) and its domain-deletion mutants with Rab5 (Q79L). Co-transformants were spotted on -Leu/-Trp, -Leu/-Trp/-His, and -Leu/-Trp/-His/-Ade media to confirm viability and interactions, respectively. **G** MBP and MBP-TECPR2_TECPR proteins were used to pull down the indicated GFP-tagged Rab5 (WT) or mutant proteins expressed in HEK293T cells. The GFP-tagged proteins were detected by IB and MBP proteins using Ponceau S staining. Densitometric analysis of GFP-Rab5 (WT) and mutant proteins, normalized to the input and direct pulldown, is shown. SE = Short Exposure; LE = Long Exposure. **H** GST and GST-Rab5 (WT) and mutants were used to pull down the MBP-TECPR2_TECPR protein. The MBP-tagged proteins were identified by IB and GST proteins using Ponceau S staining. Densitometric analysis of TECPR2_TECPR protein, normalized to the input and direct pulldown, is shown. **I** HEK293T cell lysates co-expressing indicated GFP- and FLAG-tagged proteins were immunoprecipitated with anti-GFP and IB with the indicated antibodies. The anti-GFP nanobody was visualized using Ponceau S staining. Densitometric analysis of TECPR2 (WT) and mutants, normalized to the input and direct IP, is shown. **J** Yeast two-hybrid assay of TECPR2 HSAN9-associated variants with Rab5 (Q79L). Co-transformants were spotted on -Leu/-Trp and Leu/-Trp/-His media to confirm viability and detect interactions, respectively. **K** HEK293T cell lysates co-expressing indicated GFP- and FLAG-tagged proteins were immunoprecipitated with anti-GFP and IB with the indicated antibodies. The anti-GFP nanobody was visualized using Ponceau S staining. Densitometric analysis of TECPR2 (WT) and mutants, normalized to input and direct IP, is shown. Source data are provided as a Source Data file.

that Rab5 interacts with the TECPR2_TECPR region of TECPR2 in a GTP-dependent manner.

Finally, to test whether there is direct binding of TECPR2_TECPR fragment with GTP-bound Rab5, we performed a protein-protein interaction assay using recombinantly expressed and purified proteins. As shown in Fig. 1H, the TECPR2_TECPR fragment directly bound to GST-tagged Rab5 (Q79L), and a significantly weaker interaction was observed with GST-tagged Rab5 S34N, confirming a physical interaction between the C-terminal region of TECPR2 and GTP-bound Rab5. Next, we employed ColabFold, a program that permits AlphaFold2-based predictions of protein complexes, to determine the binding interface residues between TECPR2_TECPR and Rab5[20]. Analysis of the predicted complex identified Met 1251, Ile 1256, and Glu 1299 as binding interface residues in TECPR2 (Supplementary Fig. S1B). These three residues are also highly conserved across evolution, increasing their likelihood of being relevant for TECPR2 function (Supplementary Fig. S1C). As shown in Supplementary Fig. S1D, E, mutation of residues Met 1251 and E1299 but not I1256 to alanine disrupted binding of TECPR2 to Rab5 in a yeast two-hybrid assay. Corroborating these results, co-immunoprecipitation of TECPR2 (WT) and (I1256A) mutant with Rab5 was observed, whereas the TECPR2 (E1299A) mutant failed to interact with Rab5, suggesting that residues Met 1251 and E1299 are likely to form the Rab5 binding interface in TECPR2 (Fig. 1I).

## HSAN-associated non-synonymous coding variants within the C-terminal TECPR repeats of TECPR2 disrupt its binding to Rab5

Previous studies have identified that the HSAN-associated missense clinical variants of TECPR2 map to the conserved residues within the N-terminal WD40 domain and the C-terminal TECPR repeats, suggesting that these residues regulate TECPR2 stability and function (Fig. 1A and Supplementary Fig. S1C)[15]. As we found that Rab5 directly interacts with the C-terminal TECPR repeats (935-1411 a.a.), we next evaluated the Rab5 binding potential of HSAN-associated clinical variants within this region. To this end, we created previously known non-synonymous coding variants in TECRP2: T903M, D1000Y, W1140G, and R1336W, all of which mark residues that are conserved across evolution (Supplementary Fig. S1C)[15]. AlphaMissense (AM), a technology designed to predict the pathogenicity of missense variants, showed that the TECPR2 clinical variants (D1000Y), (W1140G), and (R1336W) had high AM scores and were categorized as pathogenic variants, whereas clinical variant (T903M) had a low AM score and was categorized as a benign variant (Supplementary Table I)[21,22]. Interestingly, TECPR2 (D1000Y), (W1140G), and (R1336W) showed highly reduced or no binding to Rab5, whereas TECPR2 (T903M) continued to interact with Rab5, similar to the WT protein (Fig. 1J).

We noted that the TECPR2 variants (D1000Y), (W1140G), and (R1336W) had highly reduced expression in cell lysates compared to the WT protein, while the (T903M) variant expression was similar to WT (Supplementary Fig. S1F). The (W1140G) variant of TECPR2 did not show a band corresponding to the WT molecular weight ( ~ 180 kDa) but showed an unexplained downward mobility shift; thus, this variant was not used for further analysis. Consistent with the yeast two-hybrid assay results shown in Fig. 1J, TECPR2 variants (D1000Y) and (R1336W) were unable to immunoprecipitate Rab5, whereas co-immunoprecipitation of Rab5 was observed with the TECPR2 (T903M) variant (Fig. 1K). A previous study indicated that the non-synonymous coding variant (R1337W) in canine TECPR2 (residue R1336 in humans) is associated with juvenile-onset neuroaxonal dystrophy (NAD)[23]. Our results suggest that while the (R1336W) mutation may affect TECPR2 stability, leading to its reduced expression, the minimally expressed version is also defective in Rab5-binding, which may further contribute to the etiology of the HSAN9 disorder.

## TECPR2 localizes to early endosomes in a Rab5-dependent manner, a process disrupted in the HSAN-associated R1336W variant

Previous studies have shown that epitope-tagged TECPR2 localizes to the cytosol, and partial overlap has been reported with ER markers, including COPII coat proteins SEC24D, SEC31, and VAPB[11,14]. We were unable to assess localization of endogenous TECPR2, as the commercially available anti-TECPR2 antibodies did not detect the protein at this level of expression in multiple mammalian cell lines, including HeLa, HEK293T and hTERT-RPE1 cells. Therefore, we analyzed the localization of epitope-tagged TECPR2 constructs, ensuring that only moderately expressing cells were taken for analysis. We observed that GFP-tagged TECPR2 (GFP-TECPR2), while having a mostly cytosolic distribution, also showed punctate localization (Fig. 2A). Immunostaining of GFP-TECPR2-expressing cells with anti-Rab5 antibodies showed that the GFP-TECPR2$^+$ punctae were positive for Rab5 (Fig. 2A; Pearson's colocalization coefficient (PCC) quantification is shown in Fig. 2B). TECPR2$^+$ punctae were also positive for the Rab5 effector and the early endosomal marker EEA1 (Fig. 2A, B), while little or no colocalization was observed with the late endosomal/lysosomal markers Rab7 and LAMP1 (Supplementary Fig. S2A and Fig. 2B).

Next, to analyze whether TECPR2 colocalizes with the ER tubular network, we co-expressed TECPR2 with the ER membrane contact site protein VAPB, previously shown to interact with TECPR2[14]. GFP-TECPR2 in live cells showed a cytosolic localization with few punctate structures and was not observed to be overlapping with the VAPB-positive ER tubular network; however, a subset of GFP-TECPR2$^+$ vesicles were colocalized with VAPB. TECPR2$^+$ vesicles were also observed to be co-migrating in contact with the ER tubules, a behavior reminiscent of early endosome motility along the ER tubules (Supplementary Movie 1)[24].

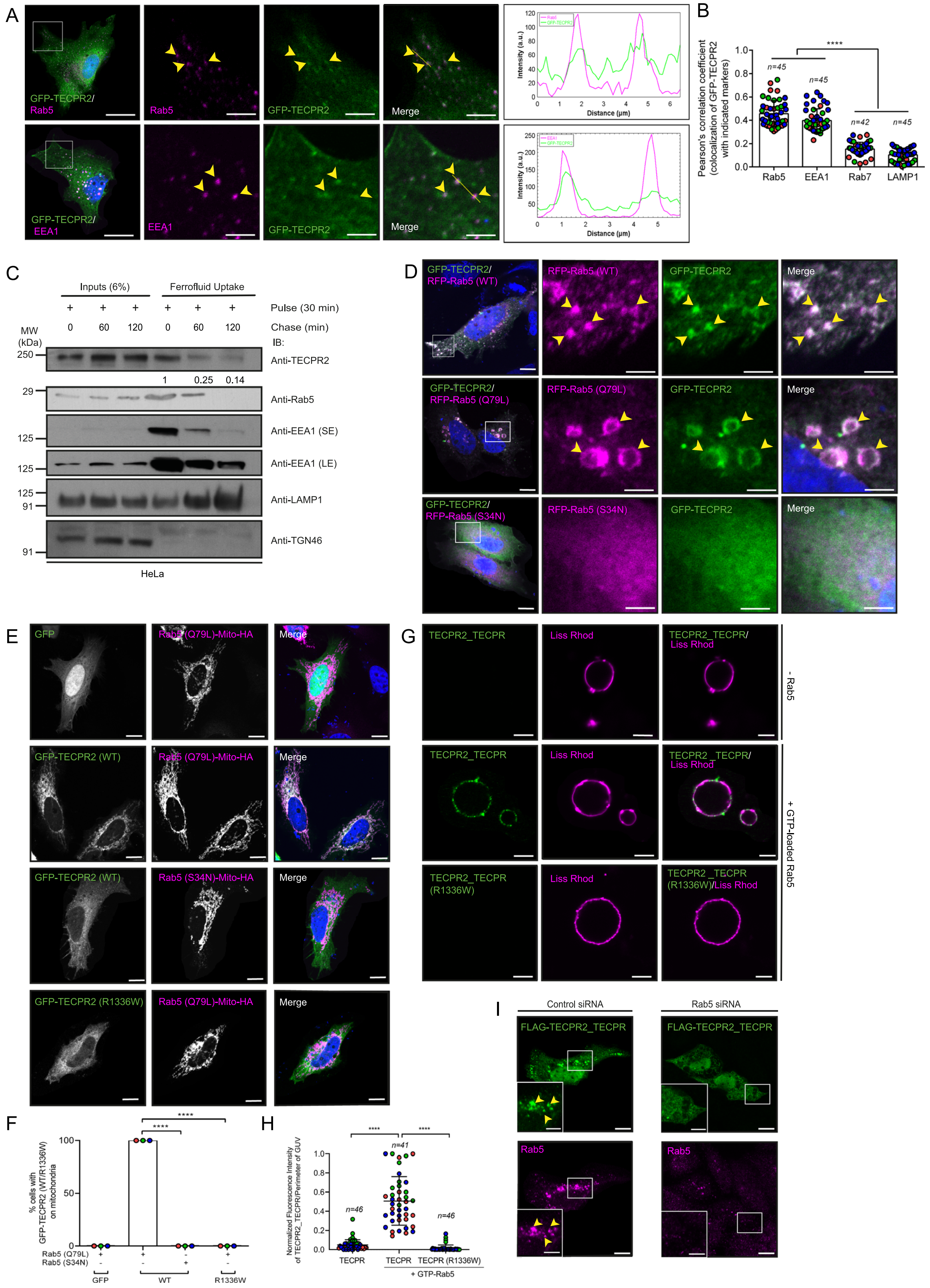

To test whether endogenous TECPR2 localizes to early endosomal fractions, we used an approach wherein cells were incubated with 10 nm paramagnetic particles (Ferrofluid [FF]), and endocytosed paramagnetic particle-containing vesicles were isolated from cell homogenates at different time points post-incubation[9,25]. As shown in Fig. 2C, the early endosomal proteins, including Rab5 and EEA1, were enriched in the pulse-only sample, and their levels steadily decreased upon chase for 60 min and 120 min, whereas the late endocytic/lysosomal marker, LAMP1, showed a reverse trend, indicating maturation of the FF-loaded endosomes with increasing time points of chase. We did not observe the presence of Golgi marker TGN46 in any of the fractions, indicating that the fractions were endocytic compartments. We found that TECPR2 was enriched in the early endosomal fractions as compared to the late endosomal

**Fig. 2 | Rab5 recruits TECPR2 on early endosomes, a process disrupted in the HSAN-associated TECPR2 (R1336W) variant. A** Representative confocal micrographs of HeLa cells transfected with GFP-TECPR2 and immunostained for endogenous Rab5 and EEA1. The line profiles indicate fluorescence intensity along the yellow line for both channels. Arrowheads in the insets denote the colocalized pixels. Scale bars: 10 μm (main); 5 μm (inset). **B** Quantification of the Pearson's colocalization coefficient for GFP-TECPR2 with the indicated markers is shown. *n* denotes the total number of cells analyzed, and the error bar represents the mean ± SD from three independent experiments. Experiments are color-coded, and each dot represents the individual data points ($^{****}p < 0.0001$; unpaired two-tailed Student's *t*-test). **C** HeLa cells were treated with the indicated siRNA and incubated with ferrofluid (FF) for 30 min at 37 °C, followed by a chase in complete media for the indicated time. The FF-containing compartments were purified at the indicated time points, and immunoblotted (IB) for the indicated proteins. SE = Short Exposure; LE = Long Exposure. Densitometric analysis of TECPR2, normalized to the input, is shown. **D** Representative confocal micrographs of HeLa cells co-transfected with GFP-TECPR2 and RFP-Rab5 (WT) and mutants. Arrowheads in the insets denote the colocalized pixels. Scale bars: 10 μm (main); 5 μm (inset). **E** Representative confocal micrographs of HeLa cells co-transfected with either GFP or GFP-TECPR2 (WT and R1336W) with Rab5 (Q79L and S34N)-Mito-HA and immunostained with anti-HA antibodies. Scale bars: 10 μm. **F** Quantification of the percentage of cells in which GFP-TECPR2 (WT and R1336W) was re-localized to mitochondria. A total of 16 cells were analyzed per experiment for each sample. The data shown is mean ± SD from three independent experiments. Experiments are color-coded, where each dot represents the mean value ($^{****}p < 0.0001$; unpaired two-tailed Student's *t*-test). **G** Representative confocal micrographs of Liss-Rhodamine-labeled GUVs incubated with purified TECPR2_TECPR (WT) and TECPR2_TECPR (R1336W) in the absence or presence of purified GTP-loaded Rab5. The GUVs were immunostained with anti-TECPR2 antibody (green). Scale bars: 10 μm. **H** Quantification of the fluorescence intensity of TECPR2_TECPR (WT/R1336W) per perimeter of GUV in the absence or presence of GTP-loaded Rab5. The values are represented as described for Fig. 2B, and *n* denotes the total number of GUVs analyzed. The data shown is mean ± SD from three independent experiments ($^{****}p < 0.0001$; unpaired two-tailed Student's *t*-test). **I** Representative confocal micrographs showing FLAG-TECPR2_TECPR localization in HeLa cells treated with indicated siRNA. The cells were immunostained with anti-FLAG and anti-Rab5 antibodies. Arrowheads in the insets denote the colocalized pixels. Scale bars: 10 μm (main); 5 μm (inset). Source data are provided as a Source Data file.

fractions, strengthening our conclusion that TECPR2 localizes to early endosomes (Fig. 2C).

Rab proteins direct vesicular transport by recruiting its effectors to target membranes. Next, we employed several independent approaches to test whether GTP-bound Rab5 recruits TECPR2 to early endosomes. First, co-expression of Rab5 (WT) and its constitutively dominant active mutant (Q79L) led to membrane recruitment of GFP-TECPR2, whereas in cells co-expressing the constitutively dominant negative mutant (S34N) of Rab5, TECPR2 showed a completely cytosolic distribution (Fig. 2D). Importantly, in contrast to TECPR2 (WT), the HSAN9 variants of TECPR2 that weakly interacted with Rab5, (D1000Y) or did not interact (W1140G and R1336W), remained cytosolic in the presence of Rab5 (Supplementary Fig. S2B, C). Consistent with its binding to Rab5, the HSAN9-associated variant (T903M) continued to colocalize with Rab5 (Supplementary Fig. S2B, C). The AlphaFold2-predicted Rab5-binding defective mutant, i.e., TECPR2 (E1299A), also showed a highly reduced overlap with Rab5 endosomes, suggesting that Rab5 binding is required for TECPR2 membrane localization (Supplementary Fig. S2B, C).

Second, we employed the MitoID method for Rab effector and regulator identification to test whether Rab5 is sufficient to direct TECPR2 membrane localization[18]. To this end, we expressed GFP-TECPR2 with constitutively dominant-active and dominant-negative Rab5 constructs fused to a mitochondrial-targeting sequence (Rab5 (Q79L)-mito and Rab5 (S34N)-mito). As a control, we first verified that no mitochondrial recruitment of the GFP tag by itself was observed in the presence of Rab5 (Q79L)-mito (Fig. 2E, F). GFP-TECPR2 was recruited to mitochondria in cells co-expressing Rab5 (Q79L)-mito, while no recruitment was observed with Rab5 (S34N)-mito (Fig. 2E, F). Further, the HSAN9-associated TECPR2 variant (R1336W) was not recruited to mitochondria in the presence of Rab5 (Q79L)-mito, indicating that GTP-bound Rab5 interacts with and recruits TECPR2 to intracellular membranes, and this process is disrupted by the HSAN9-associated (R1336W) mutation (Fig. 2E, F).

Next, we employed an in vitro minimal reconstitution assay to test whether Rab5 is sufficient to direct TECPR2 on membranes. To this end, constitutively active Rab5 (Q79L) was anchored on giant unilamellar vesicles (GUVs) through a covalent bond between the C-terminal cysteine residue of Rab5 and a maleimide-conjugated lipid in GUV, as recently described[26]. We confirmed Rab5 loading by immunostaining the Liss-Rhodamine-labeled GUV membranes with anti-Rab5 antibodies (Supplementary Fig. S2D). Next, we incubated the purified Rab5-binding fragment of TECPR2, i.e., TECPR2_TECPR (WT) and the Rab5-binding defective version (TECPR2_TECPR (R1336W)) with GUVs containing GTP-loaded Rab5 and evaluated TECPR2 recruitment using immunostaining with anti-TECPR2 antibodies. We found that TECPR2_TECPR (WT) was recruited to GUVs in the presence of GTP-loaded Rab5, and no recruitment was detected on GUVs without Rab5 (Fig. 2G, H). Importantly, even in the presence of GTP-loaded Rab5, TECPR2_TECPR (R1336W) was not recruited to GUVs, confirming previous observations that this HSAN9-associated TECPR2 variant does not interact with Rab5 and therefore, fails to localize to membranes (Fig. 2G, H).

We found that the epitope-tagged TECPR2_TECPR (which showed qualitatively greater binding to Rab5 than full-length TECPR2) showed a punctate localization and all the punctae were colocalized with endogenous Rab5 (Supplementary Fig. S2F). In cells with moderate to high TECPR2_TECPR expression, the Rab5 effector EEA1 appeared to be cytosolic, suggesting that TECPR2_TECPR competes with other endogenous effectors for Rab5 binding (Supplementary Fig. S2F). Consistent with the essential role of Rab5 in mediating TECPR2 membrane localization, depletion of all three isoforms of Rab5 (A, B, and C) led to a relocalization of the TECPR2_TECPR fragment from the membrane to the cytosol, corroborating that Rab5-binding is required for TECPR2 membrane association (Fig. 2I; knockdown efficiency was >90%, as confirmed by immunoblotting and shown in Supplementary Fig. S2E). Taken together, we conclude that the C-terminal TECPR repeats in TECPR2 are essential and sufficient for Rab5 binding and, consequently, for TECPR2 recruitment to early endosomes. Importantly, impaired Rab5 binding and lack of membrane localization may explain the loss-of-function phenotype of the HSAN9-associated TECPR2 (R1336W) variant.

## TECPR2 localizes to and maintains the peripheral distribution of early and recycling endosomes

To gain insights into TECPR2 function, we next decided to visualize the dynamics of TECPR2-positive early endosomes in live cells. We imaged only moderately expressing cells for this analysis, as a higher TECPR2 expression leads to the formation of enlarged and perinuclearly clustered Rab5-positive early endosomes (see Supplementary Fig. S2B for reference). We observed two different populations of TECPR2 and Rab5-positive endosomes: peripheral, smaller endosomes that showed bidirectional motility near the cell surface, and relatively larger perinuclear ring-shaped endosomes that were less mobile (Supplementary Movie 2). We also found that TECPR2$^{+}$ short tubules emanating from Rab5$^{+}$ endosomes occasionally undergo fission (Fig. 3A, B and Supplementary Movie 3). TECPR2$^{+}$ endosomes also exhibited tethering and homotypic fusion (Supplementary Movie 3). Analysis of intensity profile over time showed that TECPR2$^{+}$ endosomes occasionally underwent both fission and

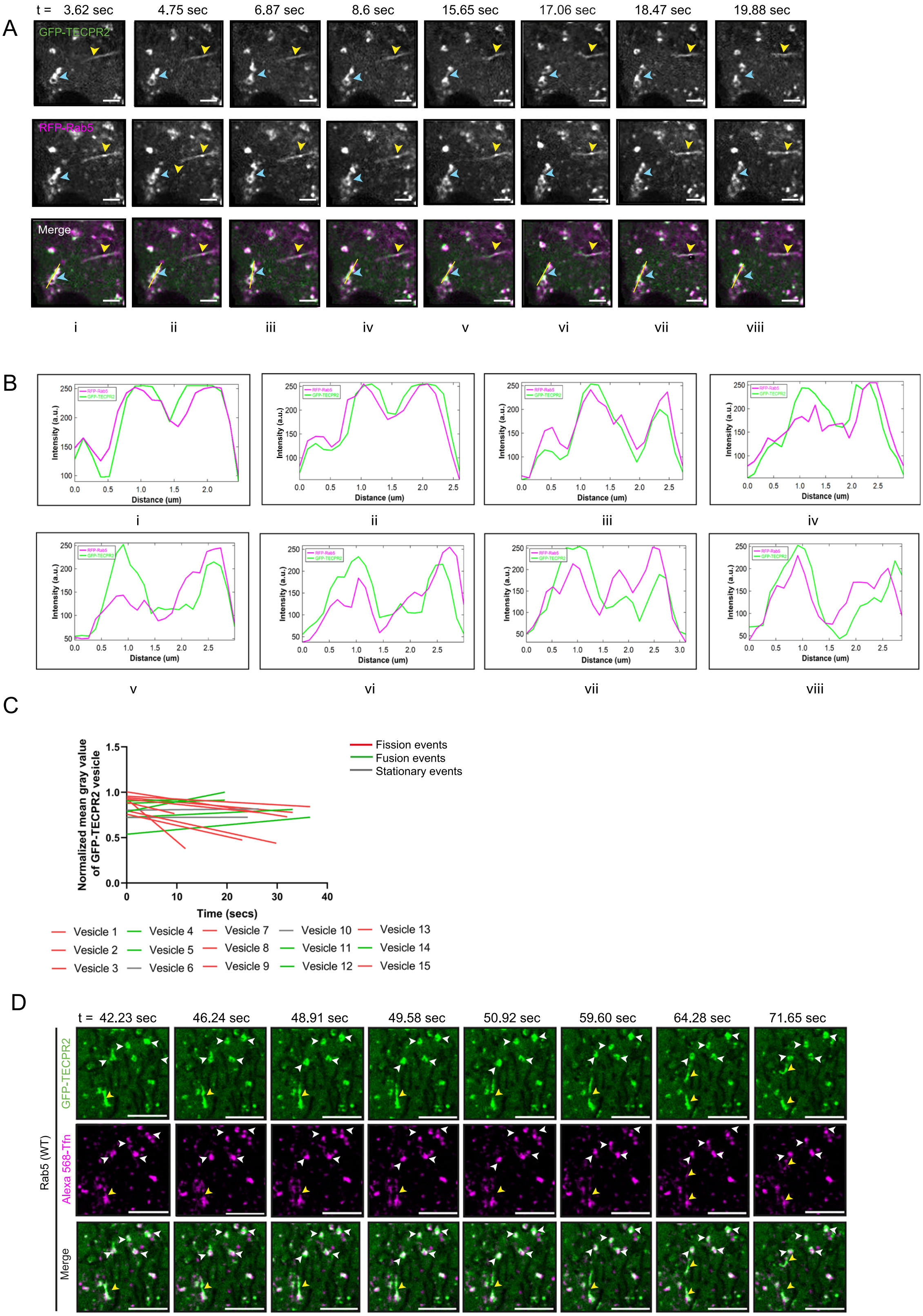

fusion (Fig. 3C and Supplementary Fig. S3). In a subset of transfected cells, we also observed TECPR2 localizes to relatively long, and stable tubules (Supplementary Movie 4). We did not observe tubulation of TECPR2 endosomes in fixed cells, likely because of poor preservation of the tubular structures upon fixation. In agreement with its lack of binding to Rab5, the HSAN9-associated TECPR2 (R1336W) variant did not show localization to vesicular or tubular membranes when co-expressed with Rab5 (Supplementary Movie 5). Next, we analyzed whether TECPR2 vesicular and tubular endosomes were accessible to endocytic cargo. To this end, we incubated TECPR2- and Rab5-co-expressing cells with labeled transferrin (Tfn-568), a cargo that recycles back to the cell surface along with its receptor. At 5 min post-internalization, Tfn-568 was present in TECPR2$^{+}$ endosomes. We also observed Tfn-568 localized on

**Fig. 3 | TECPR2-positive peripheral early endosomes are accessible to endocytosed cargo and undergo membrane remodeling, including tubulation and fission events. A, B** Live-cell imaging of HeLa cells co-expressing GFP-TECPR2 (green) and RFP-Rab5 (magenta) (see Supplementary Movie 3). The blue arrowheads indicate GFP-TECPR2- and RFP-Rab5-positive vesicles forming short tubules and undergoing fission to form two separate endosomes. The yellow arrowheads indicate GFP-TECPR2-positive tubules. Scale bars: 5 μm. **B** The line-scan analysis shows the fluorescence intensity of GFP-TECPR2 and RFP-Rab5 across the indicated endosome (marked by a blue arrowhead). **C** The graph displays the fluorescence intensities of GFP-TECPR2-positive vesicles during the fission and fusion processes. Linear regressions are shown for a total of 15 vesicles from three independent experiments. Slightly positive and negative slopes are marked in green and red, respectively, and the stationary events are indicated in gray. **D** Live-cell imaging of HeLa cells co-expressing GFP-TECPR2 (green) and untagged-Rab5 and incubated with Alexa 568-Tfn ligand (magenta) (see Supplementary Movie 6). The live-cell imaging was started after 5 min of Alexa 568-Tfn pulse. The white arrowheads indicate GFP-TECPR2 vesicles containing Alexa 568-Tfn, and one of the vesicles is undergoing elongation and eventually fission. The yellow arrowheads indicate Alexa 568-Tfn-containing GFP-TECPR2-positive tubules undergoing a fission event. Scale bars: 5 μm. Source data are provided as a Source Data file.

TECPR2$^+$ tubular endosomes, which eventually underwent fission (Fig. 3D and Supplementary Movie 6).

To gain insights into understanding TECPR2 function on the early endosomes, we next visualized the morphology and distribution of early and recycling endosomes in TECPR2-depleted cells (efficiency of knockdown as confirmed by Western blotting was >90%, as shown in Supplementary Fig. S4A). We observed a reduction in Rab5- and EEA1-positive endosomes from the cell periphery and collapse of early endosomes to the perinuclear region upon TECPR2 depletion (Fig. 4A). We also noted a partial redistribution of Rab5 to the cytosol, and a subset of Rab5- and EEA1-positive endosomes were enlarged in TECPR2-depleted cells (Fig. 4A–C). The phenotype of enlarged early endosomes was partially rescued upon re-expression of WT TECPR2 (Fig. 4A–C). Notably, TECPR2-depleted HeLa cells had significantly reduced cell spreading compared to control cells (compare cell spreading in Fig. 4A control siRNA versus TECPR2 siRNA). Therefore, to quantify the altered positioning of early endosomes, we measured the fractional distance of Rab5 and EEA1 signal intensities from the cell center, a method independent of the cell area[27]. Indeed, TECPR2-depleted cells exhibited a significant shift in early endosome distribution towards the perinuclear region (Fig. 4A, D). The effect on early endosome distribution was rescued by the re-expression of TECPR2 (WT), indicating that this phenotype was specifically due to TECPR2 depletion (Fig. 4A, D). Next, we analyzed the distribution of Rab5 effectors, Rabenosyn-5, and APPL1 in TECPR2-depleted cells. APPL1 endosomes form a distinct Rab5-positive sorting compartment that exchanges cargo via fusion and fission with EEA1$^+$ endosomes[28]. We observed that in TECPR2-depleted cells, while Rabenosyn-5 showed a partial redistribution to the cytosol and perinuclear positioning, APPL1-positive endosome size and distribution appeared similar to the control (Supplementary Fig. S4E, F). We validated this phenotype of altered size and distribution of early endosomes by depleting TECPR2 using two independent siRNA oligo sequences, as well as in other cell lines, including HEK293T and hTERT-RPE1 (Supplementary Fig. S4B–D and S4G–I). The defect in cell spreading was also evident in TECPR2-depleted cells treated with different siRNA oligos, as well as in hTERT-RPE1 and HEK293T cell lines (Supplementary Fig. S4G–K).

We next determined whether TECPR2 depletion affects recycling endosome morphology and distribution, as TECPR2-positive endosomes were accessible to cargo such as the transferrin receptor (TfR). TECPR2-depleted cells showed perinuclear accumulation of the peripheral TfR$^+$ endosomes, which were recycling endosomes as indicated by their overlap with Rab11 (Fig. 4E, G and Supplementary Fig. S4J and L). TfR endosomal distribution was rescued upon re-expression of WT TECPR2, indicating that this phenotype was specifically due to TECPR2 depletion (Fig. 4E and G). TECPR2-depleted cells also showed a reduction in Rab11$^+$ tubules, suggesting that TECPR2 regulates the formation of tubular recycling endosomes (Fig. 4F). We also found that SNX1, which marks the early endosomal sorting vesicles that mediate cargo trafficking towards the TGN, also relocalized and collapsed in the perinuclear region (Fig. 4H and Supplementary Fig. S4K). Furthermore, TECPR2 depletion led to a significant increase in colocalization of SNX1 with ESCRT-0 subunit HRS, which defines the degradative subdomain of early endosomes (Fig. 4H, I).

In summary, we found that TECPR2-positive vesicles and tubules were accessible to recycling cargo, such as transferrin, and that the depletion of TECPR2 resulted in altered morphology and positioning of early and recycling endosomes. We found an increased overlap of SNX1, a sorting adaptor for cargo retrieval on early endosomes, with ESCRT-0 subunit HRS, which binds ubiquitinated cargo for their subsequent endolysosomal degradation in TECPR2-depleted cells. To understand how TECPR2 depletion impacts the late endocytic pathway, we visualized the distribution of the late endocytic markers Rab7 and LAMP1 in these cells. Notably, we observed enlargement of late endosomes and lysosomes marked by Rab7 and LAMP1 (Supplementary Fig. S4M). Based on these observations, we hypothesize that depletion of TECPR2 might lead to impaired cargo recycling to the cell surface and increased membrane traffic towards the degradation pathway, causing a higher influx of membranes and cargo towards the late endosomal and lysosomal compartments.

## TECPR2 mediates retrieval of the β1 integrin receptor from lysosomal degradation

To investigate the role of TECPR2 in cargo recycling, we followed the constitutive recycling of the TfR in control and TECPR2-depleted cells. We observed a modest but consistent reduction in steady-state surface levels of TfR by approximately 20% in TECPR2-depleted cells (Supplementary Fig. S5A). Accordingly, there was a reduced uptake of Tfn-568 ligand in TECPR2-depleted cells. When normalized to the pulse-only signal, we found a modest decrease of ~20% in Tfn recycling upon TECPR2 depletion at 20 and 30 min of chase in complete media (Supplementary Fig. S5B). Tfn-568-containing endosomes were also collapsed in the perinuclear region, similar to the observed steady-state distribution of TfR and Rab11 in TECPR2-depleted cells (Supplementary Fig. S5C and also see Fig. 4E). At 60 min of chase, TfR recycling was similar in control and TECPR2-depleted cells, suggesting that TECPR2 does not play a major role in TfR recycling (Supplementary Fig. S5B).

A consistent phenotype of TECPR2 knockdown was their reduced spreading, as compared to control cells (Supplementary Fig. S6A, B). Quantification of the surface area of control and TECPR2-depleted cells revealed a ~1.6-fold decrease in the surface area of TECPR2-depleted cells (Supplementary Fig. S6B). As cell spreading is mediated by integrin-dependent focal adhesion (FA) formation and FA connections to the extracellular matrix, we analyzed the FAs morphology and number upon TECPR2 depletion. To this end, we first quantified the number of FAs (labeled by paxillin) in control and TECPR2-depleted cells after reseeding them for 90 min post-trypsinization on fibronectin-coated coverslips. Indeed, there was a significant decrease in the number of FAs and in cell spreading upon TECPR2 depletion as compared to the control (Fig. 5A, B). To gain insights into the dynamics of FAs upon TECPR2 knockdown, we performed the nocodazole-washout assay wherein FAs, stabilized by nocodazole-mediated microtubule depolymerization, were observed for their regrowth during the washout phase, which is dependent on microtubule-mediated FA disassembly and reassembly. As expected, nocodazole-

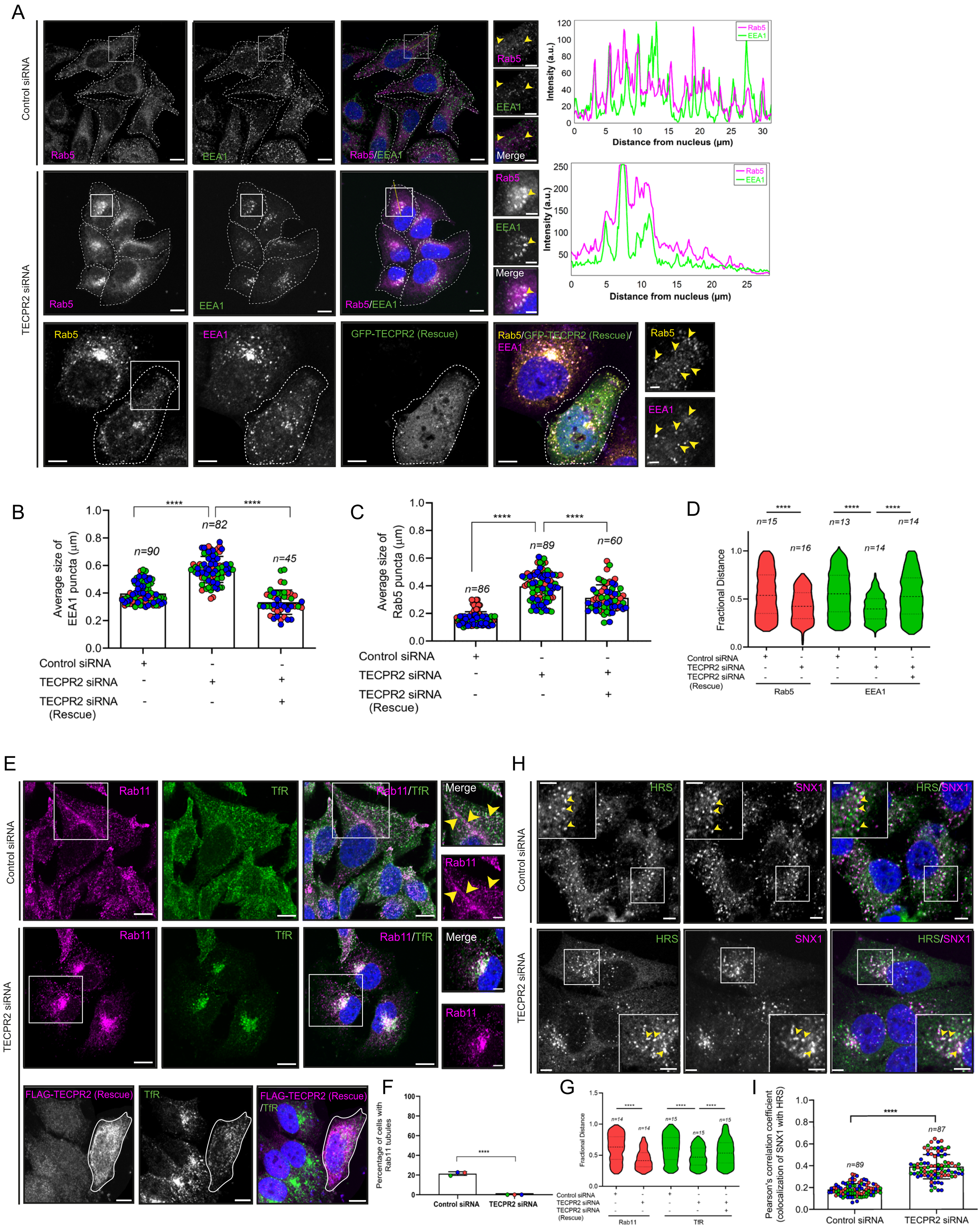

treated control cells showed stabilized or large FAs as compared to untreated cells. During the first 30 min of the washout phase, we observed disassembly of the FAs (quantified by the percentage area of paxillin per cell), followed by FA reassembly between 60- and 120-min post washout (Fig. 5C, D). Expectedly, TECPR2-depleted cells showed smaller focal adhesions under basal conditions, which were stabilized upon nocodazole treatment. While disassembly of FAs was observed during the first 30 min of the washout phase, FA reassembly by 120 min post-washout was significantly delayed upon TECPR2 depletion (Fig. 5C, D). Consistent with a lack of FA assembly, TECPR2-depleted cells also showed reduced actin cables or stress fibers that were prominently observed in the control cells during the FA reassembly phase (Fig. 5C).

To gain insights into the impaired FA assembly, we investigated whether TECPR2 regulates integrin trafficking, specifically, recycling of endocytosed integrin from early endosomes. To this end, we assessed

**Fig. 4 | TECPR2 localizes to and maintains the peripheral distribution of early and recycling endosomes.** **A** Representative confocal micrographs of HeLa cells treated with the indicated siRNA that were untransfected or transfected with a GFP-tagged TECPR2 (rescue construct) followed by immunostaining with anti-Rab5 and anti-EEA1 antibodies. Cells are highlighted with a white line to visualize the cell edges. Arrowheads in the insets denote the individual endosomes in the two channels. The line-scan analysis shows the fluorescence intensity of both channels along the yellow line drawn in the merge image. Scale bars: 10 μm (main); 5 μm (inset). **B, C** Quantification of average puncta size of EEA1 (**B**) and Rab5 (**C**) from experiments such as that shown in panel (**A**). The values are represented as described for Fig. 2B. The error bar represents mean ± SD from three independent experiments ($^{****}p < 0.0001$; unpaired two-tailed Student's *t*-test). **D** Quantification of early endosome distribution represented as fractional distance of Rab5 and EEA1 vesicles from experiments such as that shown in panel (**A**). The thin horizontal dashed line indicates the interquartile range, and the thick dashed line indicates the median of the data. *n* denotes the total number of cells analyzed from three independent experiments ($^{****}p < 0.0001$; unpaired two-tailed Student's *t*-test). **E** Representative confocal micrographs of HeLa cells treated with the indicated siRNA that were either left untransfected or transfected with a FLAG-tagged TECPR2 (rescue construct), followed by immunostaining with anti-TfR, anti-Rab11, and anti-FLAG antibodies. Arrowheads in the insets indicate Rab11-positive tubules. Scale bars: 10 μm (main); 5 μm (inset). **F** Quantification of the percentage of HeLa cells treated with the indicated siRNA in which Rab11-positive tubules were observed. A minimum of 93 and 75 cells were analyzed for control and TECPR2 siRNA-treated samples, respectively. The values are represented as described for Fig. 2F. The error bar represents mean ± SD from three independent experiments ($^{****}p < 0.0001$; unpaired two-tailed Student's *t*-test). **G** Quantification of the recycling endosome distribution represented as fractional distance of Rab11 and TfR vesicles from experiments such as that shown in panel (**E**). The values are represented as described for Fig. 4D, and *n* denotes the total number of cells analyzed from three independent experiments ($^{****}p < 0.0001$; unpaired two-tailed Student's *t*-test). **H** Representative confocal images of HeLa cells treated with the indicated siRNA and immunostained with anti-SNX1 and anti-HRS antibodies. Arrowheads in the insets denote co-localized pixels. Scale bars: 10 μm (main); 5 μm (inset). **I** Quantification of the Pearson's colocalization coefficient of SNX1 and HRS in HeLa cells treated with indicated siRNA. The values are represented as described for Fig. 2B. The error bar represents mean ± SD from three independent experiments ($^{****}p < 0.0001$; unpaired two-tailed Student's *t*-test). Source data are provided as a Source Data file.

---

the surface levels of active Itgβ1 (integrin β1) in control and TECPR2-depleted cells. As shown in Supplementary Fig. S6C, the steady-state surface levels of active Itgβ1 were reduced by ~25% upon TECPR2 depletion. Next, we employed an antibody-based recycling assay to measure the kinetics of endocytosed active Itgβ1 recycling in control and TECPR2-depleted cells. We found a significant ~1.8-2-fold decrease in the ratio of surface to internal Itgβ1 levels upon TECPR2 depletion as compared to the control, indicating that the delay in focal adhesion reassembly is likely due to the impaired recycling of Itgβ1 in TECPR2-depleted cells (Fig. 5E, F). The colocalization analysis revealed that the internal non-recycled pool of Itgβ1 was present in $HRS^+$ endosomes in TECPR2-depleted cells, while the colocalization with Rab5 and EEA1 was reduced (Fig. 5G, H). As mentioned above, HRS, a subunit of ESCRT-0, marks the degradative subdomain of early endosomes from where cargo is sorted in intraluminal vesicles for their eventual degradation.

Previous studies have shown that defects in retrieval of Itgβ1 receptors from early endosomes lead to their trafficking and degradation in endolysosomes[29]. To explore whether the non-recycled pool of Itgβ1 is targeted for lysosomal degradation upon TECPR2 depletion, we measured Itgβ1 colocalization with SiR-Lysosome, a probe that labels active hydrolase (cathepsin D)-containing compartments. We observed increased colocalization of Itgβ1-containing endosomes with SiR-Lysosome over time in TECPR2-depleted cells, as compared to control (Supplementary Fig. S6D, E and Supplementary Movie 7). We then measured the total levels of Itgβ1 in cells treated with and without lysosomal V-ATPase inhibitor BafA1 (Bafilomycin A1) to investigate whether Itgβ1 is lysosomally degraded upon TECPR2 depletion. Indeed, we observed that mature β1 integrin levels (mol. wt. ~130 kDa) were significantly reduced upon TECPR2 depletion. The precursor form of Itgβ1 (~100 kDa) did not show a significant change upon TECPR2 depletion. BafA1-treatment of TECPR2-depleted cells showed rescue of the mature β1 integrin levels, indicating that Itgβ1 is degraded in lysosomes upon TECPR2 depletion (Fig. 5I, J and Supplementary Fig. S6F).

We corroborated the observed lysosomal degradation of integrins by visualizing Itgα5 (the α5 subunit of integrin heterodimerizes with Itgβ1) colocalization with LAMP1 under BafA1 treatment. A significantly increased colocalization of Itgα5 and LAMP1 was found in BafA1-treated TECPR2-depleted cells as compared to control, suggesting that TECPR2 regulates retrieval of endocytosed active Itgα5β1 heterodimers from degradation for their recycling back to the cell surface (Fig. 5K, L). To understand whether TECPR2 regulates recycling of other receptors as well, we analyzed the status of epidermal growth factor receptor (EGFR), which, in the absence or low concentration of its ligand (EGF), is sorted for recycling from early endosomes to the plasma membrane[30]. We found that surface and total levels of EGFR were reduced upon TECPR2 depletion, which was partially rescued upon Bafilomycin A1 (BafA1) treatment, suggesting that TECPR2 may regulate constitutive recycling of receptors that are actively retrieved from a lysosomal degradation fate and recycled to the cell surface (Supplementary Fig. S6G–I).

Taken together, these observations suggest that Rab5 recruits TECPR2 on early endosomes for efficient retrieval of receptors, such as α5β1 integrin, from the lysosomal degradation pathway, ensuring recycling of integrins back to the cell surface for FA assembly and proper cell spreading. TECPR2 may also regulate constitutive recycling of EGFR, but this requires exploration in future studies.

### TECPR2 interacts with integrin sorting adaptor SNX17 and regulates its localization to Rab5-positive endosomes

Previous studies have shown that knockdown of sorting nexin (SNX) 17, the sorting adaptor that binds to the NPxY motifs on Itgβ1 and Itgβ5 tails, leads to a defect in Itgβ1 retrieval from the lysosomal degradation pathway, similar to the phenotype observed upon TECPR2 depletion[29,31]. Notably, SNX27, which is closely related to SNX17 (both are members of the SNX-FERM family), has been reported as a potential binding partner of TECPR2[11,14]. Consistent with a previous report, we found a decrease in Itgβ1 stability upon SNX17 depletion, and this effect was more pronounced than observed upon TECPR2 depletion[29]. Itgβ1 levels in co-depletion of SNX17 and TECPR2 were similar to SNX17 depletion alone, suggesting that both proteins may play a role in the same pathway of integrin recycling, although SNX17 may regulate integrin recycling independent of TECPR2 as well (Fig. 6A).

To understand whether TECPR2 regulates SNX17 function in cargo recycling, we investigated endogenous SNX17 localization on $Rab5^+$ early endosomes in control and TECPR2-depleted cells. Notably, SNX17 punctate localization and its colocalization with Rab5 were significantly reduced upon TECPR2 depletion (Fig. 6B–D). Importantly, GFP-tagged SNX17 recruitment on endocytosed Itgβ1-containing early endosomes was reduced upon TECPR2 depletion (Fig. 6E, F and Supplementary Movie 8). This reduction of SNX17 on the $Itgβ1^+$ endosomes upon TECPR2 depletion prompted us to investigate whether TECPR2 interacts with and regulates SNX17 localization on early endosomes. TECPR2 and SNX17 were colocalized on endocytosed Itgβ1-containing endosomes (Fig. 7A and Supplementary Movie 9), and both proteins also colocalized on specific membrane subdomains with Rab5 in cells

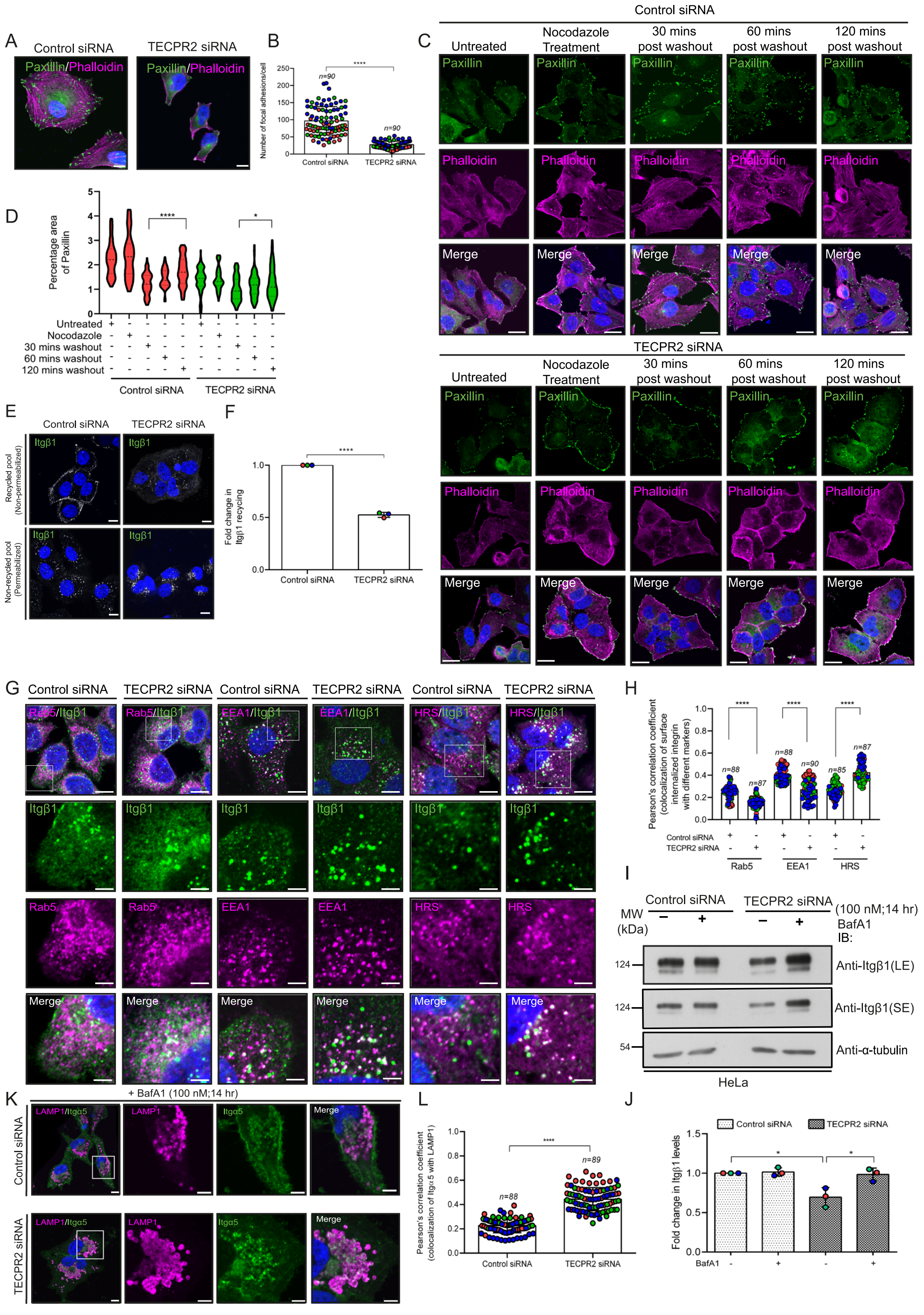

expressing the constitutively active form of Rab5 (Q79L) (Supplementary Fig. S7A). The expression of the constitutively active form of Rab5 (Q79L) leads to an increase in early endosome size, enabling better resolution of the membrane subdomains in diffraction-limited microscopy.

To test whether TECPR2 interacts with SNX17, we performed a GST pulldown assay using GST or GST-SNX17 as bait. As shown in Fig. 7B and Supplementary Fig. S7B, we found that both overexpressed and endogenous TECPR2 interact with SNX17. Next, to determine which region of TECPR2 binds to SNX17, we expressed C-terminal and N-terminal domain deletion mutants of TECPR2 with Halo-tagged SNX17 (Halo-SNX17). We found that SNX17 colocalized with TECPR2_TECPR (935-1411 a.a.) but not with the N-terminal region (1-944 a.a.), indicating that SNX17 likely interacts with the C-terminal TECPR repeat-containing region (Supplementary Fig. S7C). We found direct binding of GST-tagged SNX17 to the MBP-tagged TECPR2_TECPR

**Fig. 5 | TECPR2 mediates retrieval of the β1 integrin receptor from lysosomal degradation.** **A** Representative confocal micrographs of HeLa cells treated with indicated siRNA, followed by trypsinization and re-seeding on fibronectin. Cells were stained with anti-paxillin antibodies and phalloidin. Scale bar: 10 μm. **B** Quantification of the number of focal adhesions per cell from experiments such as those shown in the panel (**A**). The values are represented as described for Fig. 2B. The error bar represents mean ± SD from three independent experiments ($^{****}p < 0.0001$; unpaired two-tailed Student's *t*-test). **C** Representative confocal micrographs of HeLa cells treated with indicated siRNA and incubated with or without nocodazole, followed by washout for the indicated time points. The cells were then stained with anti-paxillin antibodies and phalloidin. Scale bar: 10 μm. **D** Quantification of the percentage area of paxillin per cell from experiments such as those shown in panel (**C**). A total of 30 cells were analyzed per experiment for each condition over three independent experiments. The values are represented as described for Fig. 4D ($^{****}p < 0.0001$; $^{*}p = 0.0147$; unpaired two tailed Student's *t*-test). **E** Representative confocal micrographs of the integrin recycling assay performed on HeLa cells treated with the indicated siRNA. Scale bar: 10 μm. **F** The graph represents the fold change in the ratio of surface (recycled) to internal (non-recycled) active Itgβ1 pools observed upon TECPR2 depletion normalized to control. The total number of cells analyzed was 81 and 83 for surface integrin and 101 and 100 for internal integrin for control and TECPR2 siRNA, respectively. The data shown is mean ± SD from three independent experiments. Experiments are color-coded, where each dot represents the mean value ($^{****}p < 0.0001$; unpaired two-tailed Student's *t*-test). **G** Representative confocal micrographs of HeLa cells subjected to recycling assay as shown in panel (**E**), and immunostained with indicated antibodies. Scale bars: 10 μm (main); 5 μm (inset). **H** Quantification of the Pearson's colocalization coefficient (PCC) of the internal pool of active Itgβ1 with endosomal markers, such as that shown in panel (**G**). The values are represented as described for Fig. 2B. The error bar represents mean ± SD from three independent experiments ($^{****}p < 0.0001$; unpaired two-tailed Student's *t*-test). **I** Lysates of HeLa cells were treated with the indicated siRNA, followed by treatment with or without bafilomycin A1 (BafA1), and then immunoblotted (IB) using the specified antibodies. SE = Short Exposure; LE = Long Exposure. **J** Densitometric analysis of total Itgβ1 normalized to the loading control from experiments such as those shown in panel (**I**). The data shown is mean ± SD from three independent experiments. Experiments are color-coded, where each dot represents the mean value ($^{*}p = 0.0121$ for control and TECPR2 siRNA without BafA1 treatment; $^{*}p = 0.0264$ for TECPR2 siRNA with and without BafA1 treatment; unpaired two-tailed Student's *t*-test). **K** Representative confocal micrographs of HeLa cells treated with the indicated siRNA and with BafA1. Cells were immunostained with indicated antibodies. Scale bars: 10 μm (main); 5 μm (inset). **L** Quantification of the PCC of Itgα5 with LAMP1 from experiments such as that shown in panel (**K**). The values are represented as described for Fig. 2B. The error bar represents mean ± SD from three independent experiments ($^{****}p < 0.0001$; unpaired two-tailed Student's *t*-test). Source data are provided as a Source Data file.

fragment in a purified protein-protein interaction assay. Notably, SNX17 also showed binding to the HSAN9-associated Rab5-binding defective version (TECPR2_TECPR (R1336W)), although the binding was less as compared to the WT version (Fig. 7C). These observations suggest that TECPR2 likely has distinct binding interfaces for interactions with SNX17 and Rab5.

We envisioned that, in intact cells, the HSAN9-associated Rab5-binding defective form of TECPR2 is cytosolic and may not interact with SNX17. Indeed, we observed a reduced binding between the TECPR2 (R1336W) variant and SNX17 compared to the TECPR2 (WT) (Fig. 7D). Previous studies have shown that SNX17 interacts with the Retriever-CCC-WASH complexes, which generate branched actin-enriched subdomains on early endosomes, leading to cargo sequestration and formation of recycling transport carriers[31–33]. We found that C16orf62, a subunit of the Retriever complex, and WASH complex subunits FAM21C and Strumpellin immunoprecipitated with TECPR2 (WT). In contrast, TECPR2 (R1336W) variant showed a substantially reduced interaction with the subunits of Retriever and WASH complexes, suggesting that these interactions require TECPR2's ability to localize on early endosomes (Fig. 7D).

We next tested the hypothesis that TECPR2 acts as a linker between Rab5 and SNX17 and regulates the recruitment of integrin retrieval machinery on early endosomes. To this end, we performed live-cell imaging to visualize colocalization of Halo-tagged SNX17 with GFP-tagged Rab5 in control and TECPR2-depleted cells. As previously noted, Rab5$^+$ endosomes were reduced in number and enlarged upon TECPR2 knockdown. Moreover, in TECPR2-depleted cells, we observed a noticeably less recruitment of SNX17 on individual Rab5$^+$ endosomes when compared to the Rab5$^+$ endosomes in control cells (Fig. 7E and Supplementary Movie 10). Consistent with this, we found a significantly reduced colocalization of SNX17 and Rab5 upon TECPR2 depletion (Fig. 7E, F). Based on these findings, we tested whether SNX17 interaction with Rab5 is dependent upon TECPR2 expression. Using GST pulldown assay, we found that endogenous Rab5 and TECPR2 showed binding to GST-tagged SNX17. Importantly, Rab5 binding to SNX17 was reduced upon TECPR2 depletion, suggesting that TECPR2 acts as a linker between SNX17 and Rab5 (Fig. 7G).

Finally, to analyze endogenous SNX17 recruitment on early endosomes, we purified FF-loaded endosomes from control and TECPR2-depleted homogenates after 30 min of pulse, when the fractions are enriched for the early endosomal marker, EEA1 (Fig. 7H, I). We found a modest but significant decrease in SNX17 in the early endosome fractions, whereas no significant change in EEA1 levels were observed upon TECPR2 depletion (Fig. 7H, I). The total Rab5 levels in cell homogenates (input lane) were also reduced upon TECPR2 knockdown, an effect that was confirmed by TECPR2 depletion in multiple cell lines (Fig. 7H, I and Supplementary Fig. S7D). Our results are consistent with a previous study showing increased degradation of TECPR2 interaction partners upon its depletion, although the underlying mechanism remains to be investigated as part of future work[11].

SNX27, a member of the SNX-FERM family (as SNX17), was previously reported to be a potential binding partner for TECPR2[11,14]. We validated this interaction by GST pulldown assay, where endogenous TECPR2 showed binding to GST-tagged SNX27 but not GST (used as a control) (Supplementary Fig. S7E). Furthermore, endogenous SNX27 was co-immunoprecipitated with epitope-tagged TECPR2 (WT) but not the HSAN9-associated Rab5-binding defective form of TECPR2 (R1336W), suggesting that membrane localization of TECPR2 is required for interaction with SNX27 (Fig. 7D). Consistent with their binding, endogenous SNX27 was colocalized with GFP-TECPR2 on early endosomes (Supplementary Fig. S7F, G). Importantly, SNX27 levels in the FF-loaded early endosome fractions were reduced upon TECPR2 depletion, suggesting that TECPR2 acts as a linker for both SNX17 and SNX27 to mediate their association with Rab5$^+$ early endosomes (Supplementary Fig. S7H, I). SNX27 is a sorting adaptor for cargoes, including copper transporter ATP7A and glucose transporter GLUT1, that contain a PDZ-binding motif, which is recognized by the N-terminal PDZ domain of SNX27[34]. Depletion or knockout of SNX27 results in reduced surface levels of these cargo proteins and eventually their lysosomal degradation[34,35]. In accordance with the decreased association of SNX27 with early endosomes, we found that cell surface levels of ATP7A, an SNX27 cargo, were reduced upon TECPR2 depletion. In contrast to the SNX17- and SNX27-associated cargo receptors analysed here, lysosomal transmembrane protein LAMP1 levels were increased on the cell surface upon TECPR2 depletion, an effect also reported in a previous study (Supplementary Fig. S7J, K)[14]. It will be insightful and exciting to determine the underlying reasoning for why lysosomal cargo is missorted to the cell surface, whereas cargo destined for recycling back to the surface is missorted to endolysosomes for degradation upon TECPR2 knockdown.

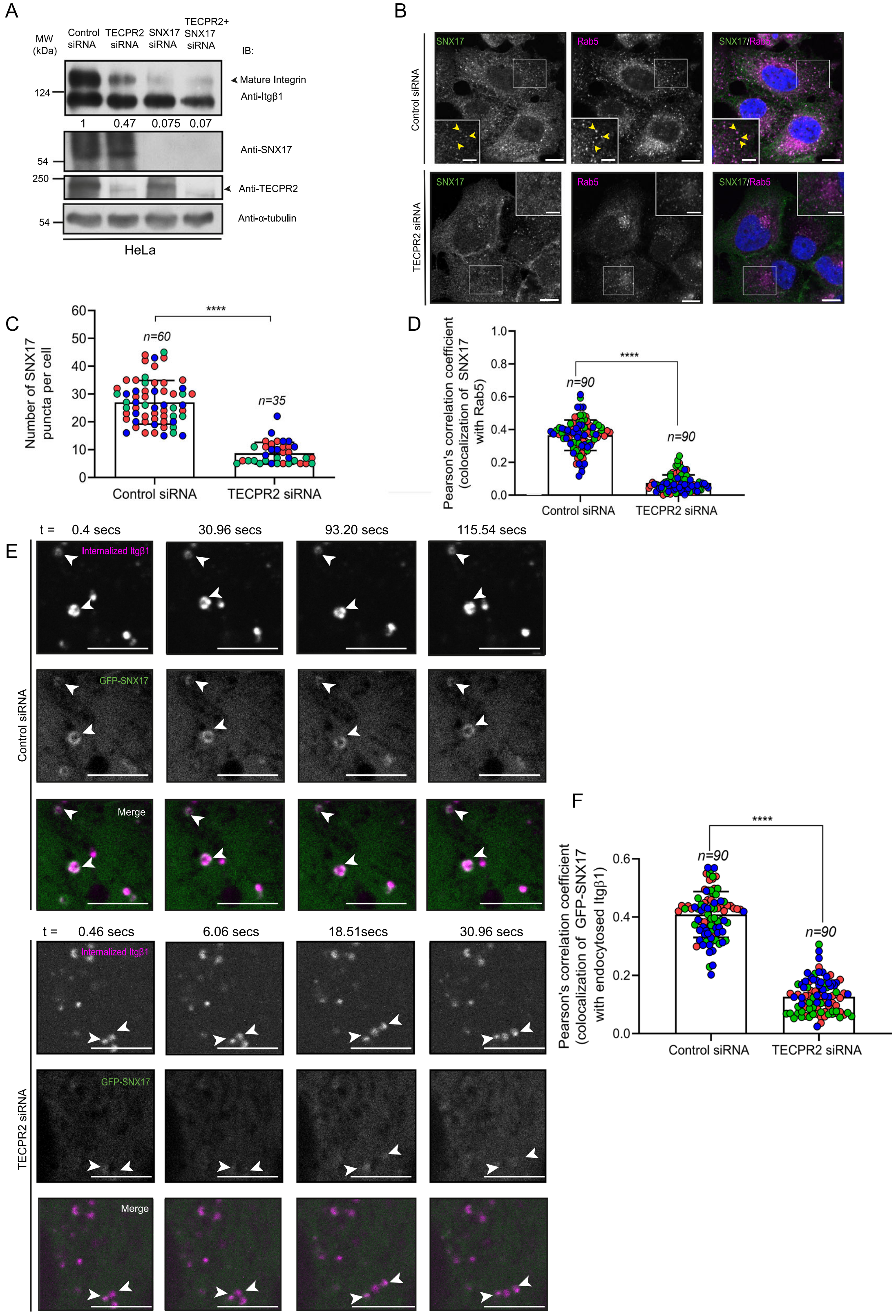

## Depletion of TECPR2 impairs localization of actin-nucleation promoting factor WASH complex on early endosomes

A crucial molecular player in the SNX17- and SNX27-mediated cargo retrieval process is the WASH complex, a Nucleation Promoting Factor (NPF) that activates the Arp2/3 complex for the generation of branched actin-enriched subdomains on early and recycling endosomes[31,33,36]. WASH is a pentameric complex consisting of WASHC1, WASHC2 (FAM21), WASHC3 (coiled-coil domain-containing protein 53 or CCDC53), WASHC4 (SWIP) and WASHC5 (Strumpellin)[36–38]. Importantly, in the context of this study, WASH complex is a known regulator of α5β1 integrin recycling to the cell surface[39]. We found that TECPR2 interacts with WASHC2/FAM21 and WASHC5/Strumpellin and was colocalized with them on membrane subdomains in cells expressing the Rab5 (Q79L) mutant (Fig. 7D and

**Fig. 6 | TECPR2 regulates membrane localization of SNX17 on early endosomes.** **A** Lysates of HeLa cells treated with indicated siRNA and immunoblotted (IB) with indicated antibodies. The signal of mature Itgβ1 is marked with an arrowhead, and the lower band indicates the precursor Itgβ1 form. Densitometric analysis of mature Itgβ1, normalized to the control siRNA-treated sample, is shown. **B** Representative confocal micrographs of HeLa cells treated with the indicated siRNA, followed by immunostaining with anti-Rab5 and anti-SNX17 antibodies. Arrowheads in the insets indicate colocalized pixels. Scale bars: 10 μm (main); 5 μm (inset). **C** Quantification of SNX17 puncta number per cell from control and TECPR2-depleted HeLa cells. The values are represented as described for Fig. 2B. The error bar represents mean ± SD from three independent experiments ($^{****}p < 0.0001$; unpaired two-tailed Student's *t*-test). **D** Quantification of the Pearson's colocalization coefficient (PCC) of SNX17 with Rab5 in HeLa cells treated with the indicated siRNA. The values are represented as described for Fig. 2B. The error bar represents mean ± SD from three independent experiments ($^{****}p < 0.0001$; unpaired two-tailed Student's *t*-test). **E** Live-cell imaging of HeLa cells treated with the indicated siRNA and expressing GFP-SNX17 (green). Before imaging, antibody-based labeling of surface Itgβ1 was performed, and cells were incubated in complete media at 37 °C to allow endocytosis of Itgβ1 (see Supplementary Movie 8). Arrowheads indicate endosomes positive for both GFP-SNX17 and endocytosed Itgβ1. Scale bar: 5 μm. **F** Quantification of the PCC of GFP-SNX17 with endocytosed Itgβ1 in HeLa cells treated with indicated siRNA. The values are represented as described for Fig. 2B. The error bar represents mean ± SD from three independent experiments ($^{****}p < 0.0001$; unpaired two-tailed Student's *t*-test). Source data are provided as a Source Data file.

Supplementary Fig. S8A). Consistent with the colocalization of WASH subunits with TECPR2, we found p16-Arc, a subunit of Arp2/3 that is recruited by WASH, also colocalized with TECPR2 on membrane subdomains in Rab5 (Q79L)-expressing cells (Supplementary Fig. S8A).

To investigate the significance of TECPR2 interaction with the WASH complex, we analyzed the localization of WASH subunits on early endosomes in TECPR2-depleted cells. We found a significant decrease in Strumpellin and WASHC1 and a modest decrease in SWIP in early endosomal membrane fractions, while no significant change was observed in FAM21C in TECPR2-depleted homogenates (Fig. 8A, B). In accordance with this, we found reduced punctate localization of Strumpellin and WASHC1, as well as reduced colocalization of WASHC1 with Rab5 in TECPR2-depleted cells (Fig. 8C–F and Supplementary Movie 11). As observed with the FF-loaded early endosomal fractions, FAM21C continued to be membrane-bound in TECPR2-depleted cells; however, it was perinuclearly clustered like other early endosomal proteins (Fig. 8C). In line with the observation that TECPR2 depletion does not affect FAM21C localization, previous studies have demonstrated that FAM21C membrane recruitment is dependent upon its interaction with Vps35 (a subunit of the retromer complex) and SWIP, which in turn has direct affinity for phosphoinositides PI(3,5)$P_2$ and PI3P[40,41].

To assess the status of actin nucleation on early endosomes upon TECPR2 depletion, we first investigated Arp2/3 localization on $Rab5^+$ endosomes. We observed reduced p16-Arc punctae and a significant decrease in p16-Arc colocalization with Rab5 upon TECPR2 depletion (Fig. 8G–I). The total levels of p16-Arc were not altered upon TECPR2 depletion, suggesting that TECPR2 regulates the localization but not expression or stability of Arp2/3 complex subunits (Supplementary Fig. S8B). The punctate localization of phalloidin, evident in control cells, was also significantly reduced upon TECPR2 depletion (Fig. 8G). Quantification of phalloidin fluorescence levels revealed an ~1.7-fold decrease in overall labeling in TECPR2-depleted cells, supporting the conclusion that TECPR2 regulates branched actin filament formation on early endosomes (Supplementary Fig. S8C).

We also visualized endosomal actin indirectly by live-cell imaging of actin capping protein CapZ (Supplementary Movie 12), which has been previously shown to interact with Rab5 and preferentially localize to early endosomes[42]. CapZ is a constitutive heterodimer of two closely related subunits, α and β and binds to the barbed ends of actin filaments to prevent their elongation[43]. CapZ also promotes nucleation in branched actin networks by regulating NPF tethering on the capped actin filament ends[44]. We found reduced punctae of CapZβ and a corresponding increase in its cytosolic localization upon TECPR2 depletion (Fig. 8J, K and Supplementary Movie 12). It is plausible that CapZ dynamically associates with early endosomes by binding to Rab5 and barbed ends of branched actin filaments. As Rab5 levels and Arp2/3-mediated actin nucleation on early endosomes are reduced upon TECPR2 depletion, this may lead to a reduced CapZ localization on early endosomes. Taken together, these findings suggest that TECPR2 regulates the retrieval of cargoes that are selected through recognition of a sorting motif sequence and through the formation of a branched actin network on early endosomes. In contrast, TECPR2 depletion does not affect recycling of cargo, such as TfR that traffics via a WASH complex (and therefore actin)-independent bulk recycling pathway, as shown in previous studies[45,46].

## TECPR2 knockdown in zebrafish induces defects in hatching and motility and an altered morphology of neuromuscular junctions

To elucidate the role of TECPR2 in vivo, we used zebrafish as a model organism to study the effects of its depletion at the organismal level. The zebrafish genome encodes two transcripts for *tecpr2* (*tecpr2*-202 encoding a protein of length 1358 a.a. and *tecpr2*-201 encoding a protein of length 1308 a.a.), which are 96.3% identical. The sequence identity and similarity between the human and zebrafish Tecpr2 longer isoform are 53.6% and 64.3%, respectively, and with the Tecpr2 shorter isoform are 55.4% and 66.3%, respectively. Importantly, we found that Tecpr2 (shorter isoform) interacted with the Rab5 ortholog in zebrafish, suggesting that this interaction is conserved across vertebrate evolution (Fig. 9A). Furthermore, the (R1234W) mutation, which is orthologous to the residue (R1336W) in human TECPR2, disrupted binding to the zebrafish Rab5 ortholog, indicating that the region and mode of Rab5 binding in TECPR2 is likely conserved across different vertebrate species (Fig. 9A, Supplementary Fig. S9A, and Supplementary Table IV for sequence alignment of TECPR2 and Rab5 in different vertebrate species). We observed the expression of *tecpr2* transcripts in zebrafish embryos at the one-cell stage, which sharply decreased 24 hours post-fertilization (hpf) and gradually increased between 72 and 96 hpf (Fig. 9B). The *tecpr2* expression showed a peak at 4 days post-fertilization (dpf), a time when the larvae are freely swimming and feeding. Whole-mount in situ hybridization analysis revealed that *tecpr2* was expressed in 0 dpf embryos; a faint expression in the brain and retina was observed at 1 dpf; at the forebrain-midbrain boundaries at 2 dpf; in the brain, retina, and anterior myotomes at 3 dpf; in the brain, swim bladder, and heart at 4 dpf; and *tecpr2* expression was observed in the brain, myotomes, and retina of 5 dpf embryos (Fig. 9C, sense probe was used as a control). The zebrafish embryos were sectioned and probed for *tecpr2* expression at different time points during zebrafish development, which also confirmed the presence of the gene from the single-cell stage until the last time point tested, i.e., 5 dpf. The sections showed *tecpr2* expression in the trunk region, a place where the neuromuscular junctions are being developed (Supplementary Fig. S9B).

As a first step towards characterizing its function, we explored whether Tecpr2 is essential during zebrafish embryonic development through a knockdown approach. To address this, we depleted both zebrafish Tecpr2 isoforms by targeted gene knockdown using morpholino (MO)-based antisense oligonucleotides against *tecpr2*-201 and -202 transcripts in single-cell stage embryos. The knockdown efficiency of the morpholinos was determined using GFP reporter constructs containing MO-target sequences that were co-injected into

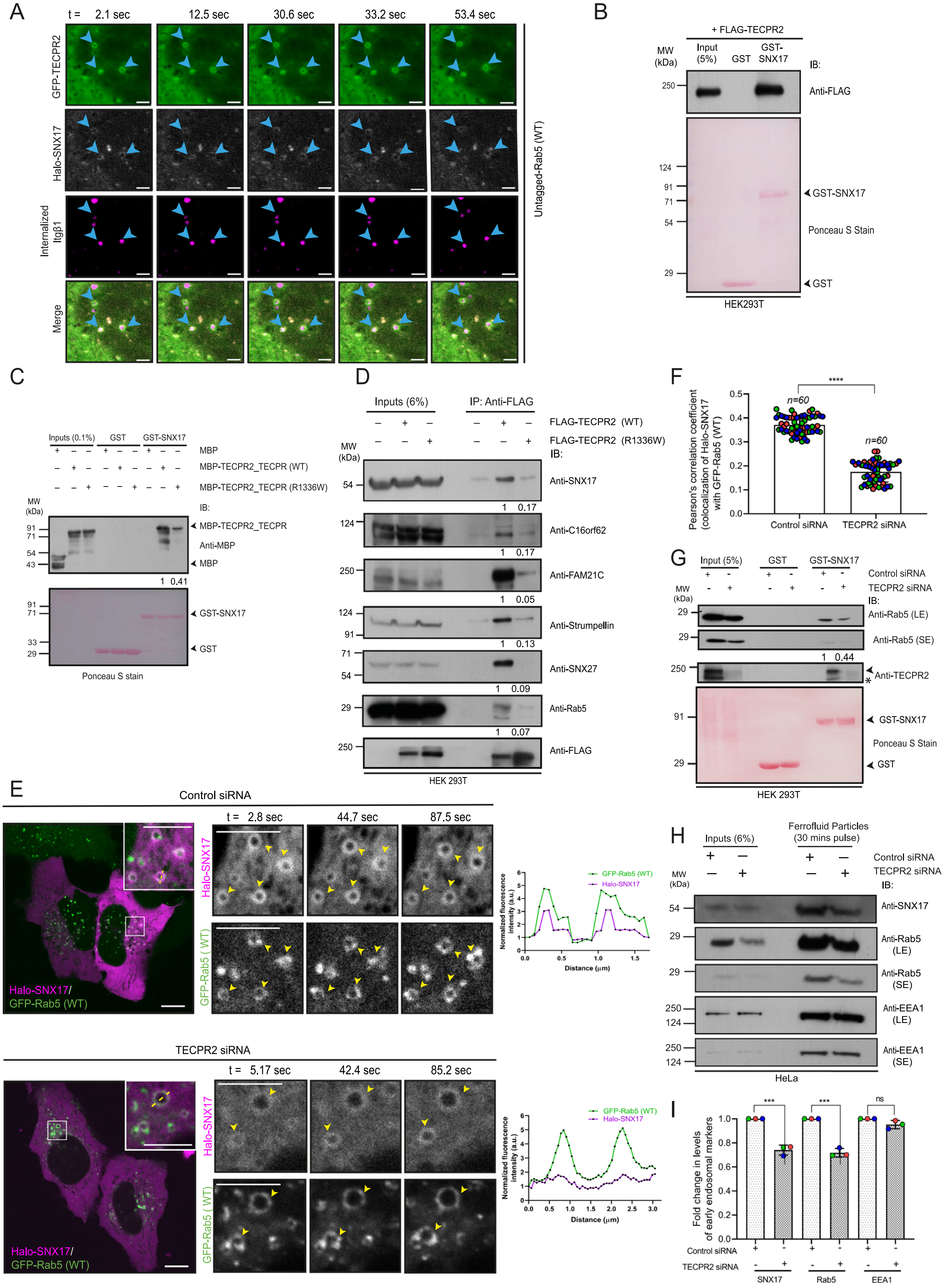

embryos along with their respective MO. Embryos injected with the control morpholino were used as controls. As shown in Supplementary Fig. S9C, control embryos demonstrated GFP expression in 100% of the embryos, whereas almost no expression of the GFP reporter was observed in embryos co-injected with either MO-*tecpr2* 201 or MO-*tecpr2* 202, confirming the efficiency of MO in knocking down gene expression.

We next assessed embryo survival and any morphological changes in zebrafish one-cell-stage embryos injected with control or combined *tecpr2* (201 and 202) MO. Compared to the control MO-injected embryos, the majority of the *tecpr2* (201 and 202) MO-injected embryos (at 0.25 mM and 0.5 mM concentrations of injected morpholinos) did not survive at 24 hpf (Fig. 9D). Furthermore, the surviving *tecpr2* (201 + 202) morphants displayed a severe hatching defect

**Fig. 7 | TECPR2 directly interacts with SNX17 and regulates the association of SNX17 with Rab5-positive endosomes. A** Live-cell imaging of HeLa cells co-expressing GFP-TECPR2 (green), Halo-SNX17 (gray) and untagged-Rab5 (WT). Endocytic uptake of active Itgβ1 (magenta) was performed as described in Fig. 6E (see Supplementary Movie 9). Arrowheads indicate colocalized pixels in all three channels. Scale bar: 5 μm. **B** GST and GST-SNX17 were used to pull down FLAG-TECPR2 expressed in HEK293T cells. The FLAG-tagged proteins were detected by immunoblotting and GST proteins using Ponceau S staining. **C** GST and GST-SNX17 were used to pull down the MBP or MBP-TECPR2_TECPR (WT) and (R1336W) variant. The MBP-tagged proteins were detected by immunoblotting and GST proteins using Ponceau S staining. Densitometric analysis of TECPR2_TECPR protein, normalized to the input and direct pulldown, is shown. **D** HEK293T cell lysates expressing either FLAG-TECPR2 (WT) or the (R1336W) variant were immunoprecipitated with anti-FLAG and immunoblotted (IB) with the indicated antibodies. Densitometric analysis of the indicated co-immunoprecipitated proteins from HEK293T cell lysates, normalized to the input and direct IP, is shown. **E** Live-cell imaging of HeLa cells treated with indicated siRNA and co-expressing Halo-SNX17 (magenta) and GFP-Rab5 (WT) (green). Arrowheads indicate endosomes positive for Halo-SNX17 and GFP-Rab5. Scale bars: 10 μm (main); 5 μm (inset). The line-scan analysis shows the fluorescence intensity of Halo-SNX17 and GFP-Rab5 across the line drawn on the indicated endosome normalized to the background (see Supplementary Movie 10). **F** Quantification of the Pearson's colocalization coefficient of Halo-SNX17 and GFP-Rab5 (WT) in HeLa cells treated with indicated siRNA. The values are represented as described for Fig. 2B. The error bar represents mean ± SD from three independent experiments ($^{****}p < 0.0001$; unpaired two-tailed Student's *t*-test). **G** GST and GST-SNX17 were used to pull down control and TECPR2-depleted HEK293T lysates. Rab5 and TECPR2 were detected by immunblotting and GST proteins using Ponceau S staining. Densitometric analysis of Rab5, normalized to the input and direct pulldown, is shown. A non-specific band detected by the anti-TECPR2 antibody is marked with an asterisk (*). **H** HeLa cells were treated with indicated siRNA and incubated with ferrofluid (FF) for 30 min at 37 °C. The FF-containing compartments were purified and IB for the presence of indicated proteins. SE = Short Exposure; LE = Long Exposure. **I** Densitometric analysis of SNX17, Rab5 and EEA1 upon TECPR2 depletion, normalized to the input and control siRNA. The data shown is the mean ± SD from three independent experiments, such as that shown in the panel (**H**). Experiments are color-coded, where each dot represents the mean value ($^{***}p = 0.0004$ for SNX17 and 0.0002 for Rab5; ns=0.0727 for EEA1; unpaired two-tailed Student's *t*-test). Source data are provided as a Source Data file.

at 72 hpf (Fig. 9E). The *tecpr2* (201 + 202) morphants that survived at 96 hpf displayed tail curvature, decreased body length, and pericardial edema (Fig. 9F and Supplementary Fig. S9D). The *tecpr2*-201 mRNA, when co-injected with MO-*tecpr2* (201 + 202), rescued the viability, hatching defect and morphological defects of Tecpr2 depletion (Fig. 9E, F and Supplementary Fig. S9D, E). Notably, co-injection of *tecpr2*-201 (R1234W) mRNA did not rescue the embryo viability, hatching defects or the morphological defects of *tecpr2* (201 + 202) morphants, indicating that, similar to other vertebrate orthologs, the (R1234W) mutation disrupts Tecpr2 function in zebrafish as well (Fig. 9E, F and Supplementary Fig. S9E). Whole-mount immunostaining of the HA epitope confirmed the translation of the injected *tecpr2*-201 and *tecpr2*-201 (R1234W) mRNA (Supplementary Fig. S9F). Consistent with the in situ hybridization data showing *tecpr2* mRNA expression in myotomes, HA-tagged Tecpr2 (WT) was also localized to the myotomes in the trunk region of the 5 dpf embryos. The mutant *tecpr2* mRNA-injected embryos revealed a diffused expression of the HA-tagged Tecpr2 (R1234W), which is consistent with its lack of binding to Rab5 and reminiscent of the cytoplasmic expression of the human TECPR2 (R1336W) variant in HeLa cells (Supplementary Fig. S9F).

At 4 dpf, we observed impaired and suboptimal motility in *tecpr2* (201 + 202) morphants compared to that in control MO-treated embryos in response to touch stimulation (Supplementary Movie 13). Co-injection of *tecpr2*-201 mRNA, which is not targetable by the antisense MO, restored normal motility in *tecpr2* (201 + 202) morphants, indicating that the motility defects are due to the reduced availability of Tecpr2. In contrast, co-injection of *tecpr2*-201 (R1234W) mRNA did not restore movement, which is consistent with the inability of this mutant to restore embryo viability and the morphological defects of *tecpr2* (201 + 202) morphants (Supplementary Movie 13). Based on *tecpr2* gene expression in the trunk region of the embryos where neuromuscular junctions (NMJs) are being developed and our findings that the human ortholog regulates receptor recycling, we speculated that defective locomotion of *tecpr2* (201 + 202) morphants might be due to altered NMJ architecture and function, which in turn could result from a defect in recycling of receptors guiding NMJ formation.

To investigate this, we sectioned and immunostained control and *tecpr2* (201 + 202) morphants for synaptic vesicle protein (SV2), a marker for presynaptic vesicles, and Alexa 488-conjugated α-bungarotoxin (α-BTX), a probe that binds to and labels postsynaptic acetylcholine receptors (AChRs). In control morphants, we observed neuromuscular synaptic morphology (visualized by SV2 colocalizing with α-BTX) as elongated and branched structures. However, in *tecpr2* (201 + 202) morphants, the neuromuscular synaptic morphology was altered, and they appeared smaller and punctate-like, instead of elongated and branched structures (Fig. 9G). The change in the NMJ was also reflected in the percentage area of the SV2 and AChRs signals, which was significantly reduced in *tecpr2* (201 + 202) morphants as compared to the control morphants (Fig. 9G–I; see the methodology section for how the percentage area was measured). Importantly, the neuromuscular synaptic morphology was rescued in embryos rescued by co-injection of *tecpr2*-201 mRNA. Importantly, the branched and elongated NMJs were more frequent in the rescue as compared to the control, which was also reflected in the percentage area of the SV2 and AChRs signals (Fig. 9G–I). In contrast, there was no discernible rescue observed upon expression of *tecpr2*-201 (R1234W) mRNA, and neuromuscular synaptic morphology was similar to the *tecpr2* (201 + 202) morphants (Fig. 9G–I).

These observations suggest that Tecpr2 regulates the normal motility of zebrafish larvae by regulating the formation of continuous and branched neuromuscular synapses. The rescue of the phenotype by wild-type *tecpr2* but not by *tecpr2* (R1234W) mRNA injection could be likely explained by the impaired formation of neuromuscular junctions upon depletion of functional Tecpr2. Our findings suggest that the zebrafish ortholog, similar to its human counterpart, might regulate endocytic recycling of receptors and other protein components that form the NMJ.

## Discussion

Previous studies on TECPR2 have not addressed how its subcellular localization is regulated. To address this question, we performed small-scale screening of Rab G proteins that might interact with TECPR2. The motivation behind such an approach was that the Rabs, Arfs, and Arl families of small G proteins generally act as recruiting agents to bring their partners to specific intracellular compartments. We found that TECPR2 interacts with Rab5, a master regulator of cargo traffic to and from early endosomes. Based on the findings from this study, we conclude that TECPR2 is a Rab5 effector, implying that Rab5 directly interacts with and recruits TECPR2 to early endosomes (Fig. 10). We also found that the HSAN9-associated TECPR2 (R1336W) variant showed reduced binding to Rab5, and accordingly, this variant is likely not functional due to its lack of membrane binding.

A recent preprint has shown that Rab partner proteins, including Rab5 effector Rabaptin-5, can undergo liquid-liquid phase separation, allowing them to form condensates on membranes. The formation of these condensates serves to limit the Rab protein to membrane subdomains and ensure Rab functions, such as vesicle tethering and

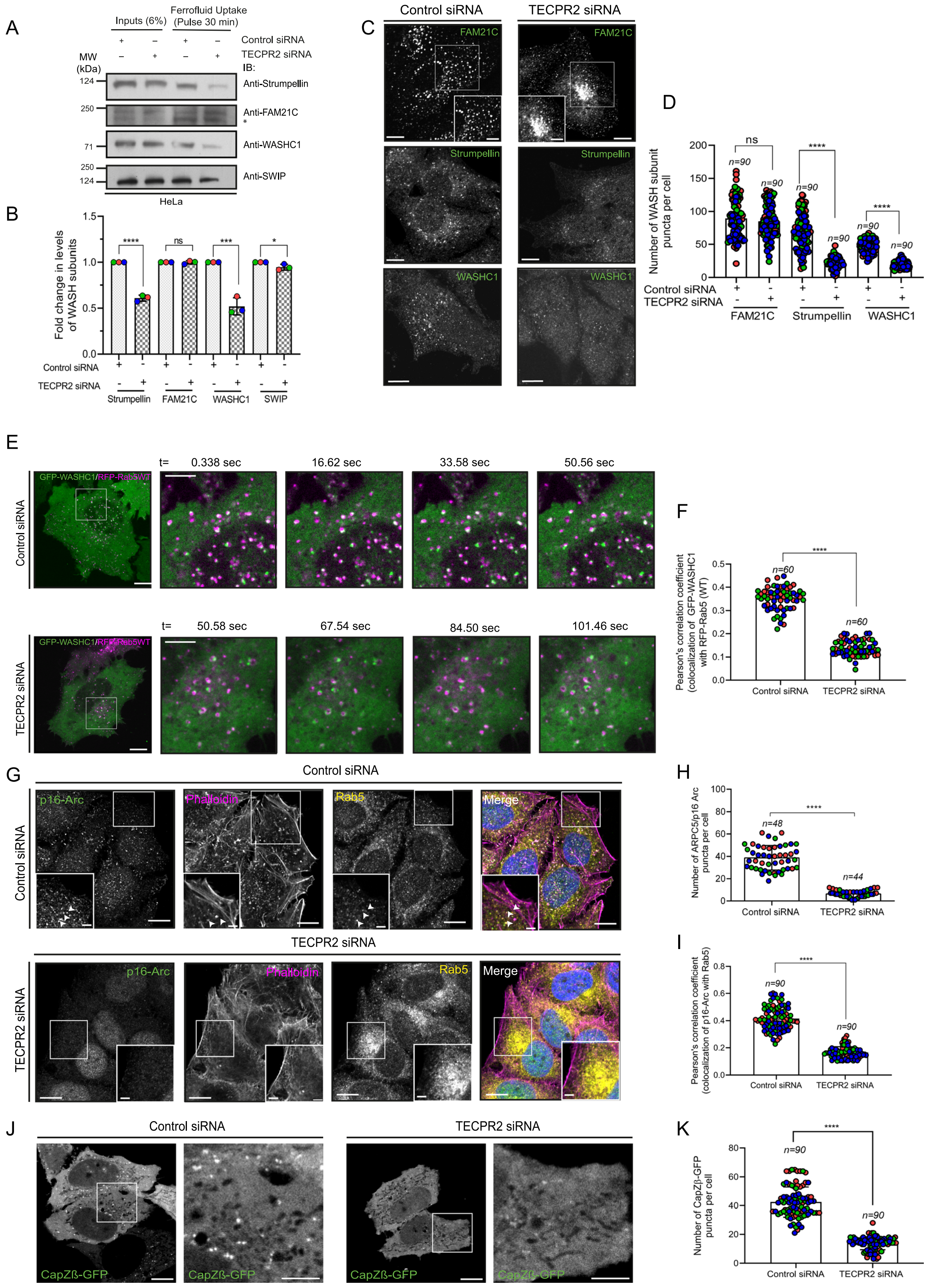

fusion[47]. Intriguingly, TECPR2 also contains a disordered region of ~400 a.a. in length (a.a. 356-790), the function of which remains unknown. It will be relevant to investigate in the future whether TECPR2 could also undergo liquid-liquid phase separation and how this feature impacts the formation of the Rab5 functional domain on peripheral endosomes. Indeed, the deletion of the first 934 amino acids from the N-terminus, which also eliminates this disordered region, leads to the formation of large and aberrant perinuclear clusters of TECPR2 and Rab5 that exclude the Rab5 effector EEA1. The functionality of these aberrant clusters in cargo retrieval has not been investigated in this work.

TECPR2-positive early endosomes were dynamic, accessible to endocytic cargo, such as TfR, and underwent frequent budding and fusion events. Occasionally, we found that TECPR2 was localized to

**Fig. 8 | Depletion of TECPR2 leads to reduced localization of WASH complex subunits on early endosomes. A** HeLa cells were treated with the indicated siRNA and incubated with ferrofluid (FF) for 30 min at 37 °C. The FF-containing compartments were purified and immunoblotted (IB) for the presence of indicated proteins. A non-specific band detected by the anti-FAM21C antibody is marked with an asterisk (*). **B** Densitometric analysis of WASH subunits upon TECPR2 depletion, normalized to the input and control siRNA. The data shown is mean±SD from three independent experiments, as shown in panel (**A**). Experiments are color-coded, where each dot represents the mean value ($^{****}p < 0.0001$; $^{***}p = 0.0009$; $^{*}p = 0.0429$; ns=0.9069; unpaired two-tailed Student's *t*-test). **C** Representative confocal micrographs of HeLa cells treated with the indicated siRNA, followed by immunostaining with anti-FAM21C, -Strumpellin, and -WASHC1 antibodies. The inset shows the perinuclear localization of FAM21C in TECPR2-depleted cells. Scale bars: 10 μm (main); 5 μm (inset). **D** Quantification of the FAM21C, Strumpellin and WASHC1 puncta numbers in HeLa cells treated with the indicated siRNA. The values are represented as described for Fig. 2B. The error bar represents mean ± SD from three independent experiments ($^{****}p < 0.0001$; ns=0.2885; unpaired two-tailed Student's *t*-test). **E** Live-cell imaging of HeLa cells treated with indicated siRNA and expressing GFP-WASHC1 (green) and RFP-Rab5 (WT) (magenta) (see Supplementary Movie 11). Scale bars: 10 μm (main); 5 μm (inset). **F** Quantification of the Pearson's colocalization coefficient (PCC) for GFP-WASHC1 with RFP-Rab5 (WT). The values are represented as described for Fig. 2B. The error bar represents mean ± SD from three independent experiments ($^{****}p < 0.0001$; unpaired two-tailed Student's *t*-test). **G** Representative confocal micrographs of HeLa cells treated with the indicated siRNA, followed by immunostaining with anti-p16-Arc (green) and anti-Rab5 (yellow) antibodies and actin labeling using Alexa Fluor-647 conjugated phalloidin (magenta). Arrowheads in the insets indicate colocalized pixels. Scale bars: 10 μm (main); 5 μm (inset). **H** Quantification of the p16-Arc puncta number in HeLa cells treated with the indicated siRNA. The values are represented as described for Fig. 2B. The error bar represents mean ± SD from three independent experiments ($^{****}p < 0.0001$; unpaired two-tailed Student's *t*-test). **I** Quantification of the PCC of p16-Arc and Rab5. The values are represented as described for Fig. 2B. The error bar represents mean ± SD from three independent experiments ($^{****}p < 0.0001$; unpaired two-tailed Student's *t*-test). **J** Representative single frame from live-cell imaging movie of HeLa cells treated with indicated siRNA and expressing CapZβ-GFP (see Supplementary Movie 12). Scale bars: 10 μm (main); 5 μm (inset). **K** Quantification of CapZβ-GFP puncta in HeLa cells treated with control siRNA and TECPR2 siRNA. The values are represented as described for Fig. 2B. The error bar represents mean ± SD from three independent experiments ($^{****}p < 0.0001$; unpaired two-tailed Student's *t*-test). Source data are provided as a Source Data file.

relatively long and stable tubular membranes. We noted the collapse of early and recycling endosomes from the cell periphery to the perinuclear region upon TECPR2 depletion. This change was most prominently observed upon visualization of recycling endosomal markers, TfR, and Rab11. The recycling endosomes were relocalized from the cell periphery to the perinuclear region, and a decrease in Rab11+ tubules was observed in TECPR2-depleted cells. TECPR2 has been previously reported to interact with and regulate the stability of BLOC (biogenesis of lysosome-related organelles complex)-1 complex that mediates biogenesis of KIF13A$^+$ and Rab11$^+$ recycling tubules[11,48]. Future studies exploring the significance of TECPR2 and BLOC-1 interaction may aid in understanding the role of TECPR2 in the biogenesis and stability of tubular recycling endosomes. TECPR2 depletion also led to an increased overlap of SNX1 (a marker for the retrograde sorting subdomain) with HRS (a marker for the degradative subdomain) on early endosomes, coupled with an increase in the size of LAMP1$^+$ late endosomal and lysosomal compartments. These findings suggest that upon TECPR2 depletion, there might be a defect in the segregation of the sorting/recycling and degradative subdomains of early endosomes (Fig. 10).

A noticeable morphological phenotype of TECPR2 depletion in multiple cell types was reduced cell spreading. We found that the dynamic assembly of FAs was impaired in TECPR2-depleted cells. This prompted us to analyze whether integrin recycling is affected upon TECPR2 depletion. Indeed, we found that TECPR2 depletion led to impaired recycling of integrins and increased lysosomal degradation, resulting in reduced integrin levels at the cell surface. To understand the mechanism by which TECPR2 regulates cargo recycling, we analyzed the localization of molecular players known to mediate integrin retrieval from the lysosomal degradation pathways. SNX17 recognizes the sorting motif in the integrin cytoplasmic tail and sorts the receptor to the recycling subdomain of early endosomes. SNX17 interacts with the retriever complex, which then interacts with the CCC and WASH complexes to mediate the recruitment of the Arp2/3 complex; this recruitment promotes branched actin polymerization, leading to the formation of tubular recycling domain and membrane fission[29,31–33].

SNX17 belongs to the SNX-FERM subfamily, similar to SNX27, which has been reported as a potential interaction partner of TECPR2 in high-throughput proteomics screening experiments[11,14]. We found that TECPR2 directly interacts with SNX17 via its C-terminal region containing TECPR repeats, and SNX17 early endosomal recruitment was reduced upon TECPR2 depletion (Fig. 10). It will be insightful in future studies to determine the binding interface residues in TECPR2 that mediate binding to SNX17 and whether HSAN9-associated variants affect binding to SNX17. While in this study we have only analyzed integrin recycling, TECPR2-depleted cells likely have defects in recycling of other cargo receptors, such as low-density lipoprotein receptor-related protein 1 (LRP1), which is also an SNX17 cargo[32,49,50].

We also found reduced levels of the WASH subunits, WASHC1 and Strumpellin, on Rab5-positive early endosomes in TECPR2-depleted cells. Accordingly, recruitment of the Arp2/3 complex on early endosomes was reduced in TECPR2-depleted cells (Fig. 10). It is relevant to note that WASH and Arp2/3-mediated actin polymerization is required for α5β1 integrin recycling to the cell surface[39]. Similar to TECPR2 depletion, WASH-knockout cells also exhibit collapse of early endosomal markers in the perinuclear region[45]. It is important to note that compared to other WASH subunits, Strumpellin levels were more noticeably decreased in the early endosomal fractions upon TECPR2 depletion. Missense mutations in Strumpellin have been reported in a form of hereditary spastic paraplegias (HSPs) known as spastic paraplegia 8 (SPG8, OMIM #603563), which is an autosomal dominant form of HSP[51–53]. Furthermore, zebrafish embryos depleted of Strumpellin show similar phenotypes to Tecpr2-depleted embryos, such as impaired motility and tail curvature[54]. An exciting avenue for further exploration will be to analyze TECPR2 interaction with Strumpellin and if the SPG8-associated point mutations in Strumpellin affect its interaction with TECPR2.

Our study does not address how TECPR2's role in cargo retrieval from early endosomes aligns with its previously described function in maintaining ERES and regulating cargo export from the secretory pathway[11,14]. We did not observe TECPR2 localization to either the ER or the Golgi membranes upon live-cell imaging in HeLa cells. Instead, epitope-tagged TECPR2 was either cytosolic or present on vesicles that were in contact with the ER tubules, a behavior reminiscent of early endosomes in contact with the ER network[24]. We observed that TECPR2-positive endosomes colocalized with VAPB, an ER membrane contact site protein, which has been previously shown to interact with TECPR2[14]. The phenotypes observed in TECPR2-depleted cells, i.e., enlarged early endosomes and lysosomes, reduced localization of actin polymerization machinery on early endosomes, and impaired cargo recycling, might be impacted by reduced ER-early endosome contact and ER-mediated endosomal tubule fission[45,55]. The defects in cargo recycling due to impaired ER- and actin-mediated endosomal tubule fission could underlie the neurodevelopmental delay and neurodegeneration pathologies in patients with loss-of-TECPR2 mutations. In strong support of this hypothesis, mutations in ER-shaping

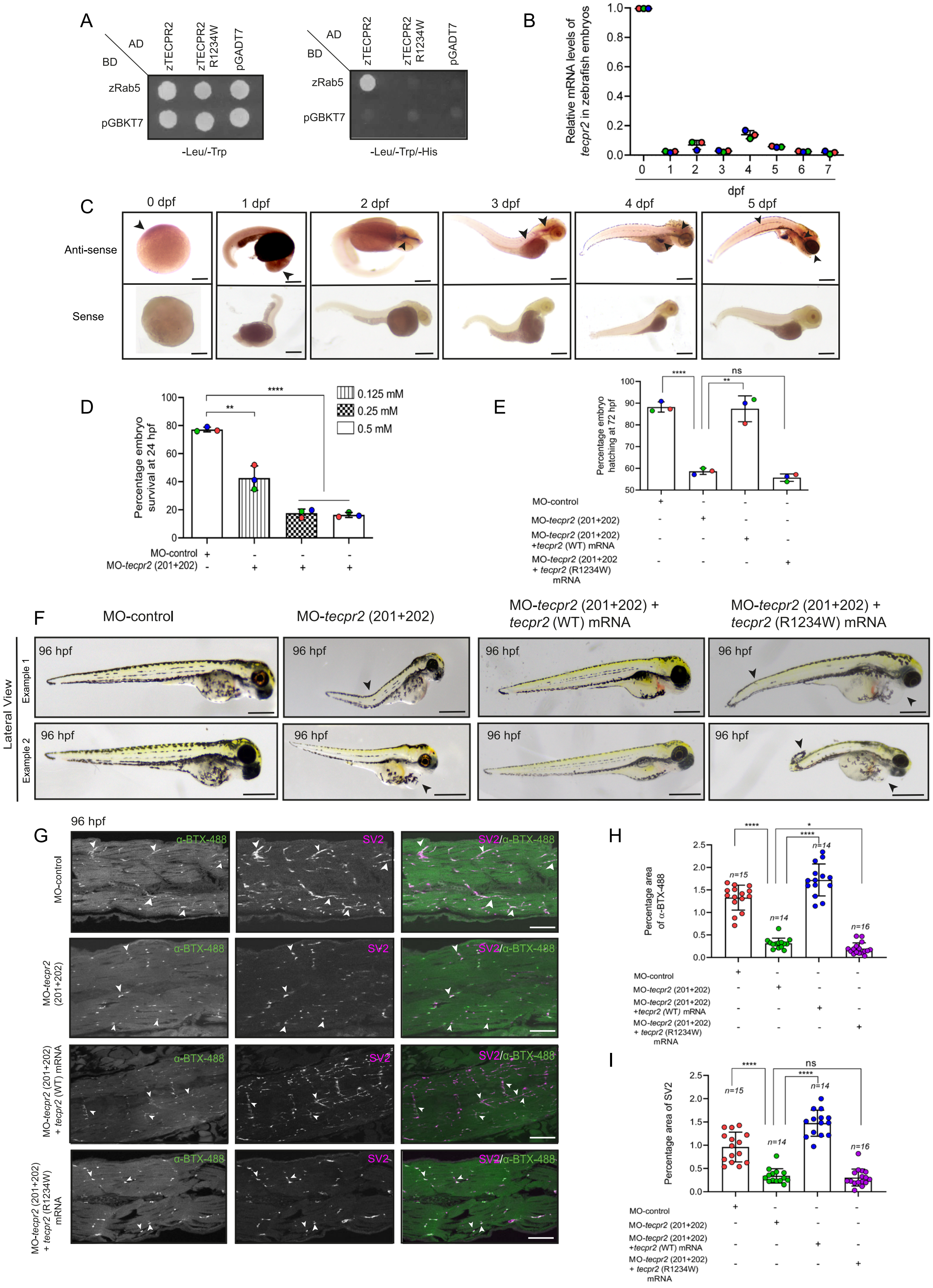

(Spastin and REEP1) and endosomal fission proteins (Strumpellin and Spastin) are associated with the most common forms of HSPs[56–58]. It is not known whether the contact sites between the ER and early endosomes also regulate ER shape and ERES formation; the latter has been shown to be reduced in TECPR2-depleted cells[11].

While we have analyzed TECPR2 function in non-neuronal cells, we predict that TECPR2 plays a similar role in regulating receptor retrieval and recycling in neurons. Loss of TECPR2 function in neurons may affect the recycling of cargo recognized by both sorting adaptors SNX17 and SNX27, as the latter protein also interacts with TECPR2 and requires TECPR2 expression for its localization to early endosomes. SNX17- and SNX27-dependent cargoes include receptors such as β1 integrin[59], β2-adrenergic receptors[60], AMPA receptors[61–63], and neuroligin-2[64], which are essential for neurite outgrowth, axon guidance, neuronal signaling, and function. Future studies on TECPR2 function and understanding the HSAN9 disorder should investigate

**Fig. 9 | Tecpr2 depletion in zebrafish results in reduced survival, hatching defects, impaired motility and altered neuromuscular synaptic morphology.** **A** Yeast two-hybrid assay of the zebrafish ortholog of TECPR2 and its (R1234W) mutant with the Rab5 zebrafish ortholog. Co-transformants were spotted on -Leu/-Trp and -Leu/-Trp/-His to confirm viability and detect interactions, respectively. **B** The graph represents *tecpr2* gene expression in zebrafish embryos at the indicated dpfs normalized to the *β-actin* gene expression. The normalized data of *tecpr2* expression at different dpfs is shown relative to the expression at 0 dpf. In each experiment, 20 embryos were analyzed. The error bar represents mean ± SD from three independent experiments, where each dot indicates the mean value. **C** Representative brightfield images of zebrafish embryos showing spatial expression of *tecpr2* transcripts at different developmental stages. The labeled sense RNA probe was used as a negative control. Scale bar: 200 μm. **D** The graph represents dose-dependent survival of zebrafish embryos at 24 hpf upon injection with the indicated morpholino. The total number of embryos analyzed was 329 for MO-control, 213 for MO-*tecpr2* (201 + 202) (0.125 mM), 197 for MO-*tecpr2* (201 + 202) (0.25 mM), and 207 for MO-*tecpr2* (201 + 202) (0.5 mM). The error bar represents the mean ± SD from three independent experiments, where each dot indicates the mean value ($^{****}p < 0.0001$; $^{**}p = 0.0025$ unpaired two-tailed Student's *t*-test). **E** The graph represents the percentage of hatched embryos after 72 hpf upon injection with the indicated morpholino. The total number of embryos analyzed was 181 for MO-control (0.5 mM), 63 for MO-*tecpr2* (201 + 202) (0.25 mM), 85 for MO-*tecpr2* (201 + 202) (0.25 mM) + *tecpr2* (rescue) WT mRNA, and 43 for MO-*tecpr2* (201 + 202) (0.25 mM) + *tecpr2* (rescue) (R1234W) mRNA. The error bar represents the mean ± SD from three independent experiments, where each dot indicates the mean value ($^{****}p < 0.0001$' $^{**}p = 0.0012$; ns=0.0866 unpaired two-tailed Student's *t*-test). **F** Lateral view of 96 hpf zebrafish embryos injected with the indicated morpholino. The arrowheads are shown to indicate the tail curvature and pericardial edema phenotype in the *tecpr2* morphant and *tecpr2* morphant injected with *tecpr2* (R1234W) mRNA. Scale bar: 200 μm. **G** Representative confocal micrographs showing embryo sections from 96 hpf control morphants, Tecpr2 morphants and Tecpr2 morphants co-injected with *tecpr2* (WT) mRNA or with *tecpr2 (*R1234W) mRNA, immunostained with Alexa 488-conjugated α-BTX (green) and anti-SV2 antibodies (magenta). Arrowheads indicate the elongated and branched neuromuscular junctions. Scale bar: 10 μm. **H, I** Quantification of the percentage area of α-BTX (**H**) and SV2 (**I**) from experiments such as that shown in panel (**G**). The *n* represents the number of sections taken from 10 embryos for each sample. The error bar represents the mean ± SD of three independent experiments ($^{****}p < 0.0001$; $^{*}p = 0.0171$; ns=0.5637; unpaired two-tailed Student's *t*-test). Source data are provided as a Source Data file.

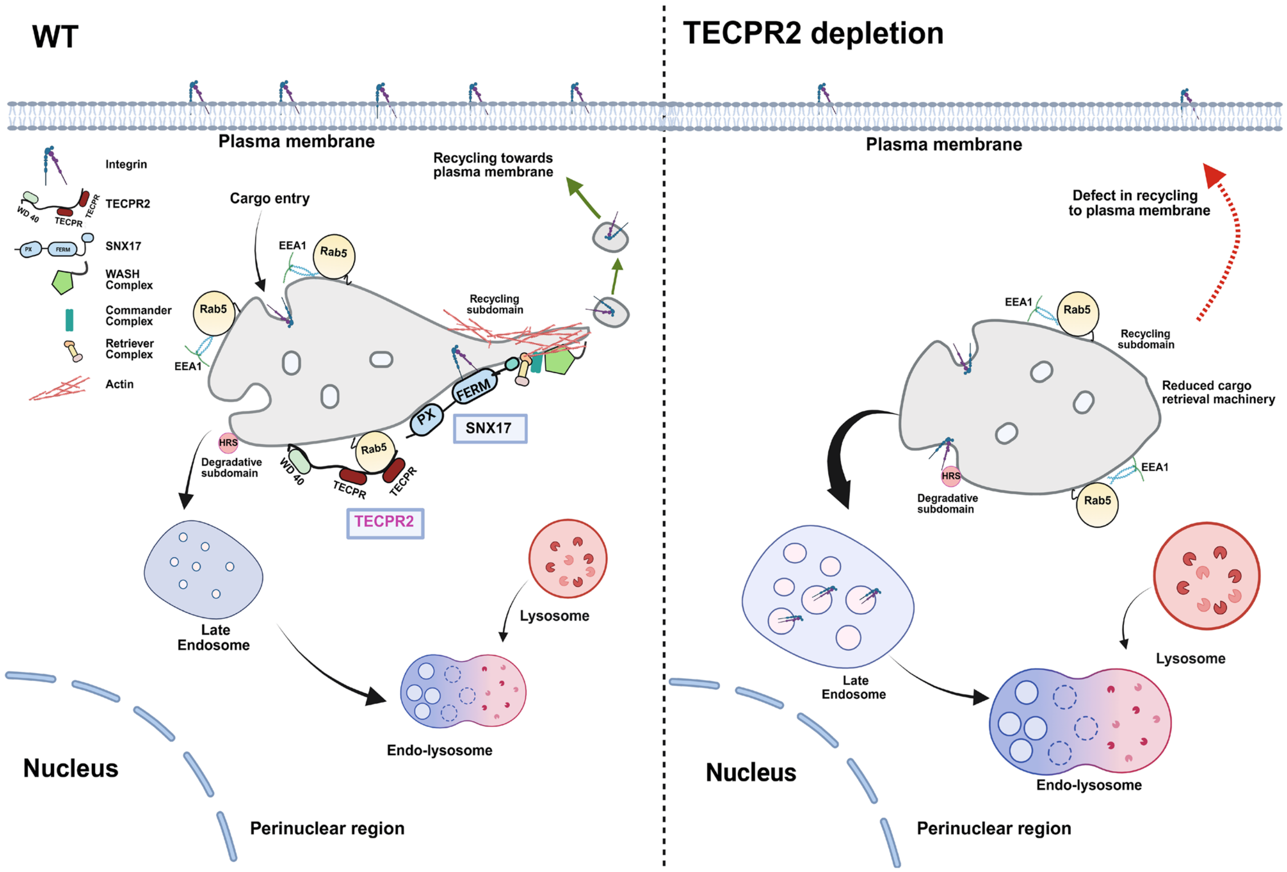

**Fig. 10 | Proposed role of TECPR2 in regulating cargo recycling to the plasma membrane.** TECPR2 is a Rab5 effector, implying that Rab5 directly interacts with and recruits TECPR2 on early endosomes. TECPR2 localizes to endocytosed active Itgβ1-containing endosomes and interacts with the Itgβ1 sorting adaptor, SNX17, and the actin nucleation-promoting factor WASH complex. TECPR2 acts as a linker between Rab5 and cargo retrieval machinery (SNX17 and WASH complex), promoting their recruitment to early endosomes, which in turn mediates the recycling of cargo (integrin) receptors to the plasma membrane. Accordingly, TECPR2 depletion leads to reduced localization of SNX17 and subunits of the WASH complex on early endosomes and impaired retrieval of integrin receptors from the lysosomal degradation pathway. WT refers to wild-type cells. Created in BioRender. Sharma, M. (2025) https://BioRender.com/qhvdmoo.

the endocytic recycling of SNX17- and SNX27-dependent cargo receptors in healthy and HSAN9-afflicted patient neurons.

As described in this study, zebrafish will be a useful in vivo model system to elucidate TECPR2 function in cargo recycling. We found that the zebrafish ortholog, similar to its human counterpart, interacts with Rab5, and the interaction was disrupted upon the introduction of the R1234W mutation, which is one of the HSAN9 disease-associated variants in human patients; the corresponding mutation in canine TECPR2 (R1337W) is associated with juvenile-onset neuroaxonal dystrophy (NAD)[15,23]. The locomotor defects observed in zebrafish embryos lacking Tecpr2 are reminiscent of the progressive spasticity observed in human patients. We found the mRNA and protein localization of Tecpr2 in zebrafish embryos to be at the myotomes, which are the sites where motor neurons from the spinal cord extend axons and form synapses with the muscle fibers. This myotome-restricted localization of the WT protein was disrupted in the Rab5-binding defective (R1234W) mutant, which was also defective in rescuing the larvae motility phenotype observed in *tecpr2* (201 + 202) morphants. It will be relevant as part of future studies to gain a better understanding of how Tecpr2 regulates neurosynaptic junction morphology and whether it plays a role in the recycling of acetylcholine receptors and other components of the NMJ. Employing zebrafish as a model, future studies can be carried out to investigate small molecules that can rescue the larvae motility phenotype observed in *tecpr2* (201 + 202) morphants.

In conclusion, this study reveals that TECPR2 is a Rab5 effector required for recycling specific cargoes back to the plasma membrane. Future studies should explore TECPR2's potential to form phase-separated condensates, which may play a role in limiting recruitment of its binding partners, Rab5 and the cargo recognition and retrieval machinery, to form an actin-rich recycling subdomain on early endosomes.

## Methods

The research conducted in this study complies with institutional biosafety guidelines, and the Institute Biosafety Committee (IBSC) of IISER Mohali approved the study protocol. All experiments on zebrafish were carried out according to established and accepted protocols of institutional biosafety and ethics committees (IISERM/SAFE/PRT/2024/034).

### Cell culture

HeLa and HEK293T (from ATCC) cells were cultured in DMEM media (Gibco) supplemented with 10% heat-inactivated fetal bovine serum (FBS; Gibco) in a humidified cell culture incubator (New Brunswick) with 5% $CO_2$ at 37 °C. hTERT-RPE1 cells (from ATCC) were cultured in DMEM/F-12 media (Gibco), supplemented with 10% FBS. For the live-cell imaging and flow cytometry experiments, cells were cultured in phenol red-free media (Gibco) supplemented with 10% FBS. All the cell lines were subcultured for not more than 18 passages and were routinely screened for the absence of mycoplasma contamination using the MycoAlert Mycoplasma Detection Kit (Lonza).

### DNA constructs, antibodies and chemicals

Supplementary Tables II and III list all the DNA constructs and antibodies used in this study, respectively. Most of the chemicals used in this study were purchased from Sigma-Aldrich. Alexa Fluor-conjugated transferrin (Tfn), phalloidin, Alexa Fluor-conjugated α-bungarotoxin (BTX), and DAPI were purchased from Molecular Probes. All the lipids used in the preparation of giant unilamellar vesicles (GUVs) were purchased from Avanti Research. Water-based ferrofluid (EMG 508) was purchased from Ferrotec Corporation. The cell-permeant HaloTag TMR ligand (G8252) and Janelia Fluor 646 HaloTag ligand (GA1120) were purchased from Promega. The avidin egg white (A2667) and TRIzol Reagent (15596026) were purchased from Invitrogen.

### Gene silencing

The siRNA oligos for gene silencing were purchased from Dharmacon (Horizon Discovery) and prepared according to the manufacturer's instructions. Transient transfection of siRNAs was performed using the DharmaFECT 1 reagent according to the manufacturer's instructions. The following siRNAs were used in this study: control siRNA, 5′-TGGTTTACATGTCGACTAA-3′; TECPR2 siRNA, 5′-CCAGATCAGTTTG CAGAAA-3′; TECPR2 siRNA oligo #2, 5′- GGAGATAGGAACATTATAA-3′ and TECPR2 siRNA oligo #3, 5′-GGAGTTTACTTCCGTGTAG-3′; and SNX17 siRNA, 5′-CCAGTGATGTCCACGGCAATT-3′. The following pool of siRNA oligos targeting all three Rab5 paralogs, Rab5a, Rab5b, and Rab5c, was used: 5′-AGGAATCAGTGTTGTAGTA-3′, 5′-GAAAGT-CAAGCCTGGTATT-3′, and 5 5'-CAATGAACGTGAACGAAAT-3′.

### Transfection, immunofluorescence and live-cell imaging

Cells grown on glass coverslips (VWR) were transfected with desired plasmids using X- tremeGENE HP DNA transfection reagent (Roche) for 16-18 h. After transfection, cells were fixed with 4% paraformaldehyde (PFA) in PHEM buffer (60 mM PIPES, 10 mM EGTA, 25 mM HEPES, 2 mM $MgCl_2$, pH 6.8) for 10 min at room temperature (RT). The cells were then blocked in blocking solution (0.2% saponin + 5% NGS in PHEM buffer) for 30 min at RT and washed three times with 1X PBS. Following blocking, cells were incubated with primary antibodies in staining solution (PHEM buffer + 0.2% saponin + 1% NGS) for 2 h at RT or overnight at 4 °C, washed three times using 1X PBS, and incubated with Alexa Fluor-conjugated secondary antibodies in PHEM + 0.2% saponin for 30 min at RT. Finally, coverslips were washed three times with 1X PBS and mounted on glass slides in Fluoromount-G (Southern Biotech). Single-plane confocal images were acquired on LSM710 confocal microscope using a 63×/1.4 NA oil immersion objective and Zen Black 2012 software (ZEISS). Super-resolution images were acquired on LSM 980 Elyra 7 super-resolution microscope equipped with a plan apochromat 63×/1.4 NA oil immersion objective and ZEN 2012 v. 8.0.1.273 (ZEISS) software. All the representative confocal images were adjusted for brightness and contrast using ImageJ/Fiji (NIH). In microscopy experiments where endogenous staining was performed, the brightness and contrast functions were adjusted to the same extent in both control and TECPR2 siRNA-treated conditions. For phase contrast imaging, cells grown on glass coverslips were fixed with 4% PFA and imaged using the Nikon Eclipse TS100 inverted microscope using a 10× objective lens.

For live-cell imaging experiments, cells were grown on glass-bottom imaging dishes (Ibidi), followed by transfection of the indicated plasmids. After transfection for 12 h, complete DMEM media was replaced by phenol red-free complete DMEM (Gibco) media, and the dish was placed in a live-cell imaging chamber that was maintained at 37 °C with a 5% $CO_2$ supply. Time-lapse imaging was performed on an Olympus IXplore SpinSR Spinning Disk Super Resolution Confocal Microscope using a 100× Apo/1.45 NA oil objective. The movies were acquired using the cellSens dimension software (Olympus) v.4.2, and the final adjustments for brightness and contrast were done using Fiji/ImageJ.

### Image analysis and quantification

**Colocalization analysis**. To analyze colocalization, images were opened in Fiji software. For quantifying the Pearson's correlation coefficient (PCC) between GFP-TECPR2 (WT) with endogenous markers or FLAG-TECPR2 mutants with GFP-Rab5, manual thresholding was performed. For this, a background subtraction was first done by selecting a small area near the nucleus; the background intensity was subtracted by using the subtract option under the "Math tool" in the "Process" menu of Fiji. For quantification of PCC of other immunofluorescence images that were showing punctate staining, the "Max Entropy" thresholding was applied. Finally, after thresholding, the JACoP plugin was used to determine the PCC.

**Quantification of size and number of puncta**. For calculating the size of Rab5, EEA1, and CapZβ puncta, the images were opened in Fiji software, and a threshold was applied by using the "Max Entropy" thresholding option. The number of punctae were then calculated by the "Analyze Particles" option in Fiji, under the "Analyze" menu. To calculate the number of punctae for SNX17 and p16-Arc, manual thresholding was applied so that only the vesicular staining was visible.

The number of puncta was then calculated by the "Analyze Particles" option in Fiji.

**Fractional distance of endosomes.** The distribution of early/recycling endosomal markers was performed by measuring the fractional distance of these endosomes. A line was drawn from the center of the cell to the cell periphery using the "line tool" of Fiji software in the confocal micrograph. The plot profile tool was then used, which selects all the endosomal marker fluorescent intensities along with their corresponding distance values on the drawn line. The background pixels and their corresponding distance values were not considered for analysis. The remaining distances corresponding to the endosomal pixels were then converted to fractional distances. This was done by dividing all these values by the total distance of the line drawn.

**Quantification of fission and fusion events.** For the calculation of fission and fusion events, GFP-TECPR2-positive vesicles near the peripheral region were chosen. A straight line was drawn along the vesicles undergoing fission or fusion, and the mean gray value was measured at each frame during the fission or fusion events. The line drawn was moved in each frame according to the movement of the vesicles in order to compensate for the small movements of the vesicles during live cell imaging. The mean gray values of each vesicle at each frame were recorded, and these values were normalized to their respective highest values. These normalized data for each vesicle was analyzed by determining their linear regression lines, and the slopes were compared to determine the fission and fusion events of the vesicles. The positive and negative slopes in the graph (Fig. 3C) were marked in green and red lines, which indicate overall fission and fusion of a single vesicle.

**Quantification of corrected total cell fluorescence.** The corrected total cell fluorescence (CTCF) values were calculated using the formula CTCF = Integrated density - (area of the selected cell X mean fluorescence of background). Images were imported into Fiji software, and the relevant parameters were calculated using the 'Measure' option under the 'Analyze' menu.

### Yeast two-hybrid assay

To perform a yeast two-hybrid assay, previously described methodology was used[65]. Briefly, the bait gene was cloned into the pGBKT7 vector in fusion with Gal4-DNA-binding domain, and the prey gene was cloned into the pGADT7 vector in fusion with Gal4-activation domain. The plasmids were co-transformed into the transformation-competent Y2H Gold strain of *S. cerevisiae* (Takara Bio Inc.). The transformants were plated on double-dropout plates that were lacking tryptophan and leucine (-Leu/-Trp) and were allowed to grow at 30 °C for 3 days to select yeast cells containing both the bait and prey plasmids. The co-transformant colonies of yeasts were plated on non-selective (-Leu/-Trp) and selective media (-Leu/-Trp/-His) or (-Leu/-Trp/-His/-Ade) to assess viability and interaction between the bait and prey proteins, respectively.

### Cell lysates, co-immunoprecipitation, and immunoblotting

For lysate preparation, cells were collected from culture dishes by trypsinization and centrifugation at 400 × *g* for 2 min. The pellet obtained was washed twice with DPBS buffer (Lonza) and lysed in ice-cold RIPA lysis buffer (10 mM Tris-Cl pH 8.0, 1 mM EDTA, 0.5 mM EGTA, 1% Triton X-100, 0.1% SDS, 0.1% sodium deoxycholate, 140 mM NaCl supplemented with 1 mM PMSF and a protease inhibitor cocktail (Sigma-Aldrich). The samples were incubated on ice for 2 min, followed by a 30 sec vortex, and this cycle was repeated five times prior to centrifugation at 16,000 × *g* for 5 min at 4 °C. The resultant clear supernatants were transferred to a new microcentrifuge tube, and using a bicinchoninic acid assay kit (Sigma-Aldrich), the amount of protein was quantified. Protein samples were prepared for immunoblotting analysis by boiling them in a 4X sample loading buffer and then loaded onto SDS-PAGE.

To perform the co-immunoprecipitation (co-IP) assay, the previously described methodology was used[65]. Briefly, HEK293T cells were transfected with the desired plasmids expressing FLAG-tag proteins. Post 20 h transfection, cells were lysed in ice-cold TAP lysis buffer (20 mM Tris-Cl pH 8.0, 150 mM NaCl, 0.5% NP-40, 1 mM $MgCl_2$, 1 mM $Na_3VO_4$, 1 mM NaF) supplemented with 1 mM PMSF and protease inhibitor cocktail, and kept on rotation (HulaMixer, Thermo Scientific) for 30 min at 4 °C. The cell lysate was centrifuged at 16,000 × *g* for 5 min at 4 °C, and the post-nuclear supernatant (PNS) was collected. PNS was incubated for 3 h at 4 °C with an anti-FLAG antibody-conjugated resin (Biolegend), followed by four washes with TAP wash buffer (20 mM Tris-Cl pH 8.0, 150 mM NaCl, 0.1% NP-40, 1 mM $MgCl_2$, 1 mM $Na_3VO_4$, 1 mM NaF, and 1 mM PMSF). Protein complexes were eluted by boiling the beads in a 4X sample loading buffer at 100 °C for 10 min. The samples were then subjected to SDS-PAGE for western blotting.

For the co-IP experiments involving the use of an anti-GFP nanobody, a recombinant GST-tagged anti-GFP nanobody was first expressed and purified from the *E. coli* Rosetta (DE3) strain using the protein purification methodology described below, and ~5 μg of the nanobody-conjugated to the glutathione beads was added to the PNS.

For performing endogenous co-IP of TECPR2 with Rab5, anti-Rab5 primary antibody (2 μg; BD Biosciences) was first incubated with the PNS for overnight at 4 °C with rotation, followed by addition of Protein A/G beads to the PNS for 3 h at 4 °C to allow the binding of primary antibody to the beads. The beads were gently washed three times with 1X PBS containing 0.1% NP-40 (Sigma-Aldrich) to remove non-specific protein binding, and samples were then prepared for western blotting analysis by boiling them in 4X sample loading buffer.

For immunoblotting, protein samples separated by SDS-PAGE were transferred onto a 0.2 μm PVDF blotting membrane (Amersham), followed by overnight incubation at 4 °C in blocking buffer (10% skim milk (BD Difco) prepared in 1X PBS containing 0.05% Tween 20 (0.05% PBST)). After washing with 0.05% PBST, the blot was incubated with a primary antibody solution prepared in 0.05% PBST for 2 hr at RT or overnight at 4 °C. The membranes were washed three times for 10 min each with 0.05% PBST and further incubated with an HRP-conjugated secondary antibody solution prepared in 0.05% PBST for 1 h at RT. Following the secondary antibody step, the membranes were washed twice for 10 min with 0.3% PBST. The blots were developed by a chemiluminescence-based method (ECL Prime Western Blotting Detection Reagent; Amersham) using medical X-ray films (Retina). For certain blots, membranes were stripped for 2 min at RT and washed three times for 5 min with 0.05% PBST before being blocked and probed with the next antibody. ImageJ software was used to perform densitometry analysis of the immunoblots.

### Recombinant protein purification, purified protein-protein interaction assay, and pulldown assay using recombinant proteins

In this study, all the His-, GST- or MBP-tagged recombinant proteins were expressed and purified from *E. coli* Rosetta (DE3) strain. For the setting up of primary cultures, a single transformed colony was inoculated into Luria–Bertani (LB) broth containing the appropriate antibiotics and incubated at 37 °C in a shaking incubator. After 12 h of incubation, 1% of primary cultures were used as inoculum to establish secondary cultures, which were then incubated at 37 °C with shaking until the absorbance at 600 nm reached 0.4-0.6. To induce protein expression, 0.3 mM IPTG (Sigma-Aldrich) was added to the cultures, followed by 16 hr of shaking incubation at 16 °C. Bacterial cultures were centrifuged at 3220×g for 10 min, washed once with 1X PBS, and resuspended in bacterial cell lysis buffer (20 mM Tris-Cl pH 8.0, 150 mM NaCl) in case of His- and GST-tagged proteins, and with buffer (20 mM Tris-Cl pH 8.0, 150 mM NaCl, 1 mM EDTA, 1 mM DTT) for MBP-tagged proteins. Both the lysis buffers were supplemented with 1 mM PMSF and a protease inhibitor tablet (Roche). The bacterial cells were lysed by sonication followed by 30 min of centrifugation at 10,062 × *g* at 4 °C. The clear supernatants were incubated with either His-cobalt resin (Thermo Scientific) for His-tagged proteins or with amylose resin (New England Biolabs) for MBP-tagged proteins, or with glutathione resin (Gbiosciences) for GST-tagged proteins on a HulaMixer for 2 h at 4 °C. To remove impurities, the resins were washed at least five to seven times with a wash buffer (20 mM Tris-Cl pH 8.0, 300 mM NaCl, 10 mM imidazole for the His-tagged proteins; 20 mM Tris-Cl pH 8.0, 300 mM NaCl for the GST-tagged proteins; and 20 mM Tris-Cl pH 8.0, 200 mM NaCl, 1 mM EDTA, 1 mM DTT for the MBP-tagged proteins).

For performing purified protein-protein interaction assay, MBP-tagged proteins were eluted from amylose resin using elution buffer (20 mM Tris-Cl pH 8.0, 200 mM NaCl, 1 mM EDTA, 1 mM DTT, 20 mM maltose monohydrate), and His-tagged proteins were eluted from the His-cobalt resin using elution buffer (50 mM Tris, pH 8.0, 300 mM NaCl, 300 mM imidazole). The eluted proteins were further concentrated using ultracentrifugal filter units (Millipore).

For obtaining purified TECPR2_TECPR (935-1411 aa) protein fragment without the MBP tag for use in GUV assays, the eluted MBP-TECPR2_TECPR (935-1411 aa) fragment was cleaved with Factor Xa enzyme (Sigma-Aldrich) by incubating with the protein at 4 °C overnight. The cleaved MBP tag and Factor Xa enzyme was then removed using size exclusion chromatography (Sephadex G-75 column; Cytiva). The purification of recombinant human Rab5a protein that was used for maleimide labeling in the GUV assay was performed as previously described[26].

To assess the binding of GST and GST-Rabs (WT or mutants) with MBP-TECPR2_TECPR (935-1411 aa) or GST and GST-SNX17 with MBP or MBP-TECPR2_TECPR (WT or R1336W), 5 μg of GST or GST-fusion proteins immobilized on glutathione-conjugated-agarose beads were incubated with 2.5 μg of MBP or MBP-fusion proteins prepared in TAP lysis buffer (20 mM Tris pH 8.0, 150 mM NaCl, 0.5% NP-40, 1 mM $MgCl_2$, 1 mM $Na_3VO_4$, 1 mM NaF, 1 mM PMSF, and protease inhibitor cocktail) for 2 h at 4 °C on a HulaMixer. Following the incubation step, beads were gently centrifuged and washed three times with TAP lysis buffer containing 0.1% NP-40. The protein complexes were eluted by boiling samples in 4X sample loading buffer at 100 °C for 10 min and are subjected to SDS-PAGE, followed by immunoblotting as described above.

For the pulldown assay using the purified recombinant GST- or MBP-tagged fusion proteins and mammalian cells as a source of lysates, the HEK293T cells alone or transfected with indicated plasmids were lysed in ice-cold TAP lysis buffer (20 mM Tris-Cl pH 8.0, 150 mM NaCl, 0.5% NP-40, 1 mM $MgCl_2$, 1 mM $Na_3VO_4$, 1 mM NaF, 1 mM PMSF, and protease inhibitor cocktail) at 4 °C for 10 min, followed by centrifugation at 16,000 × *g* for 5 min at 4 °C. The lysates were collected and incubated with GST and GST-fusion protein or with MBP and MBP-fusion protein bound to the glutathione and amylose beads, respectively, for 2-3 h at 4 °C with rotation using HulaMixer. After incubation, beads were washed at least six times with TAP lysis buffer containing 0.1% NP-40, and protein complexes were eluted by boiling samples in 4X sample loading buffer at 100 °C for 10 min before loading them onto SDS-PAGE gel and immunoblotting, as previously described.

## Purification of ferrofluid (FF)-containing endosomes

Ferrofluid (FF)-containing endosomes were purified using a previously described protocol[25]. For a fully confluent 60-mm cell culture dish, FF-containing media was prepared by adding 9 μL FF (EMG 508) to 1.5 mL of plain pre-warmed DMEM media kept at 37 °C. The suspension was sonicated for 30 sec and filter-sterilized using a 0.2 µm pore-size filter (Thermo Scientific). For uptake (pulse) of FF, the 60-mm dish containing HeLa cells were washed once with 1X PBS, and 1.5 mL of FF-containing DMEM was added to the cells for 30 min at 37 °C in a cell culture chamber. After the pulse period, cells were washed twice with 1X PBS and incubated with 10% FBS-containing DMEM media at 37 °C for the indicated time points (chase). At the end of the chase time points, cells were washed once with 1X PBS, harvested and homogenized (~20 strokes) in homogenization buffer (250 mM sucrose, 20 mM HEPES, 0.5 mM EGTA pH 7.2, and protease inhibitor cocktail) using a Dounce homogenizer (Sigma-Aldrich) on ice. The homogenates were centrifuged at 800 × *g* for 5 min at 4 °C, and the resultant PNS were collected and placed on a DynaMag-2 magnet stand (Invitrogen) for 60 min at 4 °C. The supernatants were carefully removed, and the FF-containing compartments were gently washed once with the homogenization buffer and sedimented by centrifugation. The isolated FF-containing endosomes were suspended in 4X Laemmli buffer, boiled for 10 min at 100 °C, and analyzed by SDS-PAGE and immunoblotting, as described earlier.

## Biotinylation of cell surface proteins

For surface biotinylation of proteins were performed using a previously described protocol[35]. For surface biotinylation of proteins, HeLa cells treated either with control siRNA or TECPR2 siRNA were serum starved for 1 h at 37 °C. The cells were then washed twice with ice-cold PBS, followed by labeling the surface proteins using Sulfo-NHS-SS-Biotin (Thermo Fisher) at a final concentration of 0.2 mg/mL in PBS for 30 min at 4 °C with gentle rocking. The unbound biotin was then quenched by washing the cells thrice for 5 min with PBS containing 100 mM glycine (pH 7.8). The cells were lysed on ice using the lysis buffer (50 mM Tris-Cl pH 7.4, 1 mM EDTA, 1% Triton X-100, 150 mM NaCl) supplemented with 1 mM PMSF and a protease inhibitor cocktail, and protein concentration was determined using Bicinchoninic Acid (BCA) Assay (Thermo Scientific). The equal amounts of proteins were aliquoted as inputs, and the remaining lysate were incubated with streptavidin-conjugated sepharose beads (GE Healthcare) for 2 h at 4 °C on a HulaMixer. The beads were then washed three times with ice-cold RIPA buffer, and the surface-biotinylated proteins were eluted by adding 4×Laemmli sample buffer at 95 °C for 10 min. The inputs and eluted samples were resolved by SDS-PAGE and immunoblotted as previously described.

## Flow cytometry analysis of surface protein markers

To detect the surface level of Itgβ1 in HeLa cells treated with either control siRNA or TECPR2 siRNA, cells were detached from the cell culture dish using a 5 mM EDTA solution prepared in 1X PBS and added to the cells for 15–20 min on ice. The cells were collected by gentle pipetting in a fresh microcentrifuge tube and centrifuged at 400 × *g* for 2 min at 4 °C. The cell pellets were washed once with ice-cold flow cytometry buffer (0.2% FBS in 1X PBS), followed by incubation with primary antibody solution prepared in flow cytometry buffer for 1 h on ice. The cells were washed once to remove unbound primary antibody and allowed to incubate with Alexa Fluor-conjugated secondary antibody solution made in flow cytometry buffer for 30 min on ice. Finally, the cells were washed and resuspended in flow cytometry buffer containing 1% PFA. The amount of surface receptor levels was measured by fluorescence flow cytometry using a BD FACS Aria Fusion Cytometer, and BD FACS Diva software version 8.0.1 (BD Biosciences) were used to acquire the samples. Data analysis was performed using BD FlowJo version 10.0.1.

For determining the surface level of EGFR, the above-described methodology was used with some modifications. Briefly, the cells were serum starved by incubating in DMEM media for 30 min at 37 °C, followed by fixation on ice for 15 min using 2.5% PFA solution prepared in 1X PBS. The cells were scraped out and resuspended in flow cytometry buffer containing primary antibody against EGFR to label the surface EGFR. The cells were washed once to remove unbound primary antibody and allowed to incubate with Alexa Fluor-conjugated secondary antibody solution made in flow cytometry buffer for 30 min on ice. Finally, the cells were washed and resuspended in flow cytometry buffer and analyzed by flow cytometry.

To determine the surface level of transferrin receptor (TfR) in HeLa cells treated with control or TECPR2 siRNA, the cells were serum starved in DMEM media (with 0.5% BSA) for 30 min at 37 °C. The cells were then detached from the cell culture dish by adding 5 mM EDTA solution prepared in 1X PBS to the cells for 15–20 min on ice. The cells were collected by gentle pipetting in a fresh microcentrifuge tube and centrifuged at 400 × *g* for 2 min at 4 °C. The cell pellets were washed once with ice-cold flow cytometry buffer (0.2% FBS in 1X PBS), followed by incubation with Alexa 568-Tfn (20 μg/ml) prepared in flow cytometry buffer for 1 h on ice. Finally, the cells were washed twice with ice-cold buffer and resuspended in flow cytometry buffer containing 1% paraformaldehyde (PFA) and analyzed by flow cytometry.

### Quantification of focal adhesion number

To quantify the number of focal adhesions (FA), HeLa cells grown on glass coverslips and treated with indicated siRNA were fixed and processed for immunofluorescence staining using the protocol described above. To label FA, cells were stained using an anti-paxillin antibody. To quantify the number of FA, MaxEntropy thresholding was applied to the confocal microscopy images of paxillin staining in ImageJ software. The FA number was then determined using the 'Analyze Particles' function.

To determine the number of FA after cell spreading, HeLa cells treated with indicated siRNA were trypsinized and re-seeded on glass coverslips coated with 10 μg/mL fibronectin (Sigma-Aldrich). After 90 min post-seeding, cells were fixed and stained with an anti-paxillin antibody, and the number of FA was measured as described above.

### Focal adhesion disassembly assay

The focal adhesion disassembly assay was performed using a previously described methodology[66]. HeLa cells transfected with control or TECPR2 siRNA were serum starved for 1 hr and treated with 10 μM nocodazole (Sigma-Aldrich) made in complete media for 4 hr at 37 °C to completely depolymerize the microtubules. Following nocodazole treatment, cells were washed with PBS, and pre-warmed complete media was added to the cells and incubated at 37 °C for the indicated time periods to allow repolymerization of microtubules. At the end of each time period, the cells were fixed with 4% PFA for 10 min at RT and processed for immunostaining using anti-paxillin antibody to label the focal adhesions and phalloidin to label the actin filaments. The percentage area of paxillin per cell was quantified by using the MaxEntropy thresholding and selecting the percentage area values in the Analyze Particle function in ImageJ software.

### Integrin recycling assay

Using a previously described methodology[29], a recycling assay with an antibody against active (12G10) Itgβ1 was performed. Briefly, HeLa cells growing on glass coverslips and transfected with indicated siRNA were incubated for 1 h at 37 °C with 5 μg/mL of primary antibody against active (12G10) Itgβ1 prepared in DMEM media containing 10% FBS. The cells were washed with ice-cold 1X PBS, and the surface-bound non-internalized antibodies were stripped using ice-cold citric acid buffer (pH 4.5) for 5 min. The cells were washed twice with ice-cold 1X PBS and incubated with pre-warmed 10% FBS containing DMEM media for 30 min to chase the internalized antibody. To determine the primary antibody-bound Itgβ1 pool that was recycled back to the cell surface, the cells were washed in ice-cold 1X PBS and fixed using a 4% PFA solution for 20 min on ice. After the fixation step, cells were incubated with blocking buffer (1% BSA in 1X PBS) for 10 min and stained using Alexa Fluor 488-conjugated secondary antibody prepared in blocking buffer for 30 min at RT. To determine the internal pool of primary antibody-bound Itgβ1, cells were subjected to a second acid wash step after a 30-min chase period to strip the recycled antibody from the cell surface. Cells were then fixed with 4% PFA on ice for 20 min, permeabilized with 0.1% saponin-containing blocking buffer, and stained for 30 min at RT using Alexa Fluor 488-conjugated secondary antibody and DAPI prepared in blocking buffer. Representative images were then acquired using an LSM 710 Zeiss confocal microscope.

To quantify recycling of Itgβ1 using confocal microscopy images, shell analysis was performed, as described previously[67], with some modifications. Briefly, a region of interest (ROI) covering the periphery (shape) of each selected cell was drawn using the freehand selection tool. With the clear outside function of Fiji software, Itgβ1 signals from nearby cells were removed, and the total Itgβ1 signal intensity was measured for the first ROI. The same ROI was then reduced by 2 μm, and Itgβ1 signal intensity was measured for the second ROI. Finally, surface Itgβ1 signal intensity was calculated by subtracting the intensity of the second ROI from the first ROI. For the analysis of internal Itgβ1, an ROI covering the periphery of each selected cell was drawn using the freehand selection tool. With the clear outside function of Fiji software, Itgβ1 signals from nearby cells were removed, and Itgβ1 signal intensity was measured. The ratio of the surface to internal Itgβ1 signal intensity was calculated to determine the fold change in recycling.

To assess the colocalization of endocytosed Itgβ1 with lysosomes, we performed live-cell imaging of HeLa cells treated with control or TECPR2 siRNA and incubated with a complex of anti-Itgβ1 primary antibody (clone 12G10) labeled with Alexa 488-conjugated secondary antibody on ice for 1 h to label the surface integrin. The cells were then shifted to 37 °C for 30 min to allow endocytosis of antibody-labeled Itgβ1. At the end of the 30 min period, an acid wash was given to remove the recycled pool of Itgβ1. The cells were incubated with SiR-Lysosome (1 μM; Spirochrome) to label the active lysosomes, and live-cell imaging was performed to determine the dynamics of surface endocytosed Itgβ1 with SiR-Lysosome-labeled lysosomes. To determine the colocalization of Itgβ1 with SiR-Lysosome, PCC for different time points was calculated using the JaCoP plugin of ImageJ software, as described previously.

### Transferrin recycling assay

To measure transferrin (Tfn) recycling, HeLa cells treated with control and TECPR2 siRNA were serum starved for 30 min at 37 °C by addition of DMEM media to culture dishes. The cells were washed once with 1X PBS and pulsed for 5 min at 37 °C with 20 μg/mL of Alexa 568-Tfn (Molecular Probes) prepared in DMEM media. After the pulse period, unbound or non-internalized Alexa 568-Tfn was removed by incubating the cells in citric acid buffer, pH 4.5 (0.1 M citric acid anhydrous and 0.1 M tri-sodium citrate dihydrate) for 90 sec at 37 °C. After one wash with 1X PBS, for pulse-only samples, cells were collected by trypsinization, pelleted, and resuspended in flow cytometry buffer (0.2% FBS in 1X PBS) for measurement of Alexa 568-Tfn fluorescence intensity by flow cytometry. For the "chase" samples, after the citric acid buffer (pH 4.5) wash step, pre-warmed DMEM media containing 10% FBS was added to the cells for different time periods at 37 °C. After the indicated chase period, a second citric acid buffer (pH 4.5) wash was given to cells for 90 sec at 37 °C to strip off surface recycled Alexa 568-Tfn at each time point. Cells were collected by trypsinization, pelleted, and resuspended in flow cytometry buffer (0.2% FBS in 1X PBS) for measurement of remaining intracellular Alexa 568-Tfn fluorescence intensity by flow cytometry using a BD FACS Aria Fusion Cytometer, and BD FACS Diva software version 8.0.1 (BD Biosciences) were used to acquire the samples. Data analysis was performed using BD FlowJo version 10.0.1.

To visualize Tfn recycling by microscopy, cells seeded on coverslips were processed using the above-described methodology. At the end of the pulse and chase time points, cells were fixed, processed, and imaged using a confocal microscope.

### GUV preparation and Rab5-labeling of GUVs

For GUVs, the lipid mixture was made with the following composition: DOPC (83.39 mol%), DOPE-MCC (15.55 mol%), Liss Rhod PE (0.05%), and DSPE-PEG Biotin (1 mol%). To prepare GUVs, 10 μL of the lipid mixture ( ~ 1 mM) dissolved in chloroform was placed on Indium-Tin-Oxide (ITO)-coated plates. The lipid-coated plates were then dried in a desiccator for 45 min in vacuum condition. The GUVs were then made in a swelling solution (10 mM HEPES) that was inserted inside the electroformation chamber with a syringe, and the function generator (Textronix AFG3022C) was connected to copper strips of slides. The lipid film was then electroswelled at 25 °C using a sinusoidal electric field of a sequence as previously described[68]. The GUV produced was then transferred to a 1.5 mL microcentrifuge tube coated with 5 mg/mL BSA (Sigma-Aldrich). Before labeling the GUVs with Rab5, immobilization of the GUVs was performed. An O-ring chamber attached to a glass slide was coated with avidin solution (1 mg/mL of avidin egg white (Invitrogen) prepared in 1X PBS and 5 mg/mL of BSA) for 2 hr, then washed twice with 100 μL of observation buffer (25 mM HEPES (pH 7.4) and 271.4 mM NaCl). Finally, 100 μL of observation buffer was added into the chamber, followed by the addition of 250 μL of the prepared GUVs and kept for 4 h for incubation. The human Rab5a construct that was used for maleimide labeling was generously provided by Prof. Roger Williams (MRC Laboratory of Molecular Biology, Cambridge, UK). The purification of recombinant Rab5a and its anchoring to GUVs was performed using a strategy described in a previous study[26]. Briefly, two surface-exposed cysteine residues of Rab5a were mutated to C19S and C63S to facilitate the formation of a stable thioether bond between the C-terminal cysteine residues (Cys 212 residue) of human Rab5a and maleimide-functionalized (18:1 PE-MCC) lipid vesicles. 10 μM of purified recombinant Rab5a-GTP in buffer (25 mM HEPES, 150 mM NaCl, 0.5 mM TCEP) was then added onto the immobilized GUVs and incubated at 25 °C for 4 h. The unbound Rab5 was then removed carefully by adding and taking out 100 μL of wash buffer (31.8 mM HEPES, pH 8.0, 172.7 mM NaCl, 5 mM β-mercaptoethanol, and 181.8 mM sucrose) four times. The covalently attached Rab5a-GTP was visualized by incubating GUVs with antibody against Rab5 for 2 h at 25 °C in wash buffer, followed by washing four times with wash buffer, and finally incubating with Alexa-Fluor 488 conjugated secondary antibody for 1 h at 25 °C. To visualize the recruitment of TECPR2_TECPR (WT) and TECPR2_TECPR (R1336W) onto Rab5a-GTP-bound immobilized GUV, 20 μM of these purified proteins were added to buffer (265.5 mM HEPES, 150 mM NaCl, 0.5 mM TCEP) and incubated at 25 °C for 2 h. After incubation, the unbound antibodies were removed by adding and taking out 100 μL of wash buffer. The binding of the TECPR2_TECPR (WT) and TECPR2_TECPR (R1336W) was observed by incubating with antibody against TECPR2 at 25 °C for 2 h in wash buffer, followed by washing and finally incubating with Alexa Fluor-488 conjugated secondary antibody for 1 h at 25 °C.

### Zebrafish experiments

All experiments on zebrafish were carried out according to established and accepted protocols of institutional biosafety and ethics committees (IISERM/SAFE/PRT/2024/034). Adult zebrafish were maintained at 26 °C–28 °C on a 14:10 h light/dark cycle. Embryos for all assays were obtained by natural breeding of the wild-type fish.

**Total RNA isolation extraction.** To determine the relative mRNA levels of *tecpr2* in zebrafish embryos, total RNA was isolated from 20 embryos per experiment. The embryos collected on different days post-fertilization (dpf) were washed once with RNAse-free water and then stored in 200 μL TRIzol reagent (Invitrogen) at -80 °C. The total RNA was isolated by homogenizing the embryos with a tissue homogenizer, followed by the addition of 40 μL chloroform. The mixture was allowed to stand for 3 min at RT, followed by centrifugation at 12000×g for 15 min at 4 °C. A 40 μL of upper aqueous phase was transferred to chilled tubes containing 100 μL isopropanol. The above mixture was allowed to stand at 4 °C for 15 min, followed by centrifugation and a 70% ethanol wash to get RNA pellet. The dried RNA pellet was dissolved in 10 μL of RNAse-free water. The 5 μg of total RNA was used for cDNA synthesis using an equal volume of random hexamers and oligo-dT in a Superscript III reverse transcriptase reaction (Invitrogen).

**Quantitative RT-PCR analysis.** Quantitative RT-PCR was performed with SYBR Green PCR Master Mix (Thermo Scientific) and *tecpr2*-specific primers (that bind to both *tecpr2*-201 and -202 transcripts). PCR conditions were used as per recommendations on a real-time PCR detection system (Eppendorf Master Cycler RealPlex4). The relative expression of mRNAs in embryos at different dpf was determined using the ΔΔCt method and normalized to *β-actin* mRNA levels.

*tecpr2* qRT-Fp: 5′-TGGGAGCACATTCCAGGACTTC-3′

*tecpr2* qRT-Rp: 5′-ATCCATCGGGGTCACTGCG-3′

*β-actin* qRT-Fp: 5′-GCAGAAGGAGATCACATCCCTGGC-3′

*β-actin* qRT-Rp: 5′-CATTGCCGTCACCTTCACCGTTC-3′

In situ hybridization

The 3′-end regions corresponding to *tecpr2*-201 and -202 transcripts was amplified using the primer pairs, as shown below.

Antisense probe: The reverse primer was appended with the T3 promoter region.

Fp: 5′-GGAAAGACCTGTTCTGTATTTG-3′

Rp*: 5′-ctgaattaaccctcactaaaggTTAAATCACCTCCCACTCTTCC-3′

Sense probe: The forward primer was appended with the T3 promoter region.

Fp: 5′-ctgaattaaccctcactaaaggGGAAAGACCTGTTCTGTATTTG-3′

Rp*: 5′-TTAAATCACCTCCCACTCTTCC -3′

*Lowercase shows the T3 promoter sequence.

The in situ hybridization protocol was followed using the previously described methodology[69]. The purified PCR amplicons were used for in vitro transcription with T3 RNA polymerase (New England Biolabs) and digoxigenin-labeled rNTPs (Roche, 57127421) as per the manufacturer's instructions. The DIG-labeled RNA probes were used in the whole mount in situ hybridization (WISH) for the detection of *tecpr2*-201 and -202 transcripts. The bound probes were detected with alkaline phosphatase (AP)-tagged anti-DIG antibodies (Roche). The presence of the mRNA-DIG-labeled RNA probe-AP antibody complex was detected with NBT-BCIP substrate (Roche). The representative images were captured using stereozoom microscope with a 2.5× objective (Nikon).

**Morpholino injection and rescue.** For silencing *tecpr2* expression (transcript IDs: tecpr2-201 ENSDART00000104224.5 and tecpr2-202 ENSDART00000133668.4) in zebrafish embryos, the following morpholinos (MO), purchased from Gene Tools, LLC, were used: MO control, 5′-CCTCTTACCTCAGTTACAATTTATATA-3′; MO *tecpr2*-201, 5′-GATCAATAAAAGAGGTTGCTGTGTT-3′; and MO *tecpr2*-202, 5′-CGTTTACATTGATTCTGAAGCCTAC-3′. The MO (0.25–1.0 mM) were microinjected (~1 nL) into the fertilized zebrafish eggs at a one-cell stage. For the experiments described in Fig. 9E–I and Supplementary Fig. S9D–F, 0.5 mM of control morpholino and 0.25 mM of each *tecpr2*-201 and *tecpr2*-202 morpholinos were used.

Live and dead embryos were counted manually at 24 h post-fertilization (hpf) to calculate survival percentage. Hatching percentage was determined by manually counting hatched and unhatched embryos at 72 hpf. The motility defects and phenotypic changes were assessed at 96 hpf using a stereo zoom microscope at 0.5× magnification (Nikon, SMZ45T, Michrome6 camera). The rescue of *tecpr2* morphants was done by injecting the embryo with in vitro transcribed *tecpr2*-201 mRNA (100 ng). For in vitro transcription, the CDS region of *tecpr2*-201 transcript was cloned downstream of the HA tag in pGADT7 vector. The plasmid was linearized by digestion with XhoI restriction enzyme (NEB) and was used as a template in T7-mediated in vitro transcription as per the manufacturer's instructions (MEGAscript T7 Transcription Kit) (Thermo Scientific).

**Determination of the knockdown efficiency of TECPR2 morpholinos.** To check the knockdown efficiency of MO *tecpr2*-201 and *tecpr2*-202, zebrafish embryos were injected with GFP-expressing reporter constructs (containing the *ztecpr2* MO-target sequences upstream of the GFP coding sequence in pEGFP-N1 vector) along with the respective morpholinos at a one-cell stage. The GFP expression was detected under a fluorescent stereo zoom microscope (Nikon), and images were captured using a 20× objective. All the representative confocal images were adjusted for brightness and contrast using the ImageJ software.

**Immunofluorescence staining of zebrafish embryo sections.** Zebrafish embryos at one-cell stage were injected with MO-control or MO-*tecpr2* (201 + 202) or MO-*tecpr2* (201 + 202) along with *ztecpr2* mRNA (WT or R1234W) in case of rescue experiments. The embryos at 96 hpf were fixed in 4% PFA and stored in 100% methanol at -20 °C overnight. The fixed embryos were embedded in OCT compound (Fisher HealthCare) and frozen at -80 °C. The cryosections (8-10 micron) were collected on Superfrost Plus slides (Fisher HealthCare) and air-dried overnight. The sections were permeabilized with 0.5% Triton X-100 in PBS for 30 min and blocked in 5% FBS in PBS for 1 h. The presynaptic vesicles were detected by incubating the embryos with anti-synaptic vesicle protein 2 (SV2) primary antibody (prepared in PBS containing 0.1% Triton X-100 and 5% FBS) overnight at 4 °C, followed by incubation with Alexa Fluor 568-conjugated secondary antibody for 1 h at RT. To detect postsynaptic acetylcholine receptors, the α-Bungarotoxin (α-BTX)-conjugated with Alexa Fluor 488 was prepared in PBS containing 0.1% Triton X-100 and incubated along with the secondary antibody for 1 hr at RT. The imaging of zebrafish was performed on LSM710 confocal microscope using a 63×/1.4 NA oil immersion objective and Zen Black 2012 software (ZEISS). All the representative confocal images were adjusted for brightness and contrast using ImageJ.

For quantification of the percentage area of α-BTX-488 and SV2, the images were analyzed using Fiji software, and the threshold was applied using the "Default" thresholding option. The percentage area of α-BTX-488 and SV2 were calculated by selecting the "percentage area" values in the "Analyze Particle" tool. The percentage area values were calculated as the percentage of threshold pixels in the image.

## Statistics and reproducibility

All the data are presented as the mean ± SD unless otherwise specified. Statistical significance was determined using an unpaired two-tailed Student's $t$ test (GraphPad Prism 8.0) to calculate $p$ values (****$p < 0.0001$, ***$p < 0.001$, **$p < 0.01$, *$p < 0.05$, or n.s., not significant ($p > 0.05$)). All images (microscopy images or western blots) are representative of three biological replicates with the exception of Figs. 1G, 7D, S2E, S4C-D, S7D and S8B, which are representative of two biological replicates. No statistical method was used to predetermine sample size. No data were excluded from the analyses; the experiments were not randomized; the investigators were not blinded to allocation during experiments and outcome assessment.

## Reporting summary

Further information on research design is available in the Nature Portfolio Reporting Summary linked to this article.

## Data availability

All relevant information supporting the findings of this study is presented in the manuscript and supplementary materials. Source data are provided with this paper.

## References

1. Grosshans, B. L., Ortiz, D. & Novick, P. Rabs and their effectors: Achieving specificity in membrane traffic. *Proc. Natl Acad. Sci. USA* **103**, 11821–11827 (2006).
2. Poteryaev, D., Datta, S., Ackema, K., Zerial, M. & Spang, A. Identification of the switch in early-to-late endosome transition. *Cell* **141**, 497–508 (2010).
3. Rink, J., Ghigo, E., Kalaidzidis, Y. & Zerial, M. Rab conversion as a mechanism of progression from early to late endosomes. *Cell* **122**, 735–749 (2005).
4. Naslavsky, N. & Caplan, S. Advances and challenges in understanding endosomal sorting and fission. *FEBS J.* **290**, 4187–4195 (2023).
5. Naslavsky, N. & Caplan, S. The enigmatic endosome - sorting the ins and outs of endocytic trafficking. *J. Cell Sci.* **131**, https://doi.org/10.1242/jcs.216499 (2018).
6. Zhang, M., Chen, L., Wang, S. & Wang, T. Rab7: roles in membrane trafficking and disease. *Biosci. Rep.* **29**, 193–209 (2009).
7. Khatter, D. et al. The small GTPase Arl8b regulates assembly of the mammalian HOPS complex on lysosomes. *J. Cell Sci.* **128**, 1746–1761 (2015).
8. Marwaha, R. et al. The Rab7 effector PLEKHM1 binds Arl8b to promote cargo traffic to lysosomes. *J. Cell Biol.* **216**, 1051–1070 (2017).
9. Schleinitz, A. et al. Consecutive functions of small GTPases guide HOPS-mediated tethering of late endosomes and lysosomes. *Cell Rep.* **42**, 111969 (2023).
10. Lorincz, P. et al. Rab2 promotes autophagic and endocytic lysosomal degradation. *J. Cell Biol.* **216**, 1937–1947 (2017).
11. Stadel, D. et al. TECPR2 cooperates with LC3C to regulate COPII-dependent ER export. *Mol. Cell* **60**, 89–104 (2015).
12. Behrends, C., Sowa, M. E., Gygi, S. P. & Harper, J. W. Network organization of the human autophagy system. *Nature* **466**, 68–76 (2010).
13. Oz-Levi, D. et al. Mutation in TECPR2 reveals a role for autophagy in hereditary spastic paraparesis. *Am. J. Hum. Genet* **91**, 1065–1072 (2012).
14. Nalbach, K. et al. Spatial proteomics reveals secretory pathway disturbances caused by neuropathy-associated TECPR2. *Nat. Commun.* **14**, 870 (2023).
15. Neuser, S. et al. Clinical, neuroimaging, and molecular spectrum of TECPR2-associated hereditary sensory and autonomic neuropathy with intellectual disability. *Hum. Mutat.* **42**, 762–776 (2021).
16. Fraiberg, M. et al. Lysosomal targeting of autophagosomes by the TECPR domain of TECPR2. *Autophagy* **17**, 3096–3108 (2021).
17. Tamim-Yecheskel, B. C. et al. A tecpr2 knockout mouse exhibits age-dependent neuroaxonal dystrophy associated with autophagosome accumulation. *Autophagy* **17**, 3082–3095 (2021).
18. Gillingham, A. K., Bertram, J., Begum, F. & Munro, S. In vivo identification of GTPase interactors by mitochondrial relocalization and proximity biotinylation. *Elife* **8**, https://doi.org/10.7554/eLife.45916 (2019).
19. Go, C. D. et al. A proximity-dependent biotinylation map of a human cell. *Nature* **595**, 120–124 (2021).
20. Mirdita, M. et al. ColabFold: making protein folding accessible to all. *Nat. Methods* **19**, 679–682 (2022).
21. Cheng, J. et al. Accurate proteome-wide missense variant effect prediction with alphamissense. *Science* **381**, eadg7492 (2023).
22. Tordai, H. et al. Analysis of alphamissense data in different protein groups and structural context. *Sci. Data* **11**, 495 (2024).

23. Hahn, K. et al. TECPR2 associated neuroaxonal dystrophy in spanish water dogs. *PLoS One* **10**, e0141824 (2015).
24. Friedman, J. R., Dibenedetto, J. R., West, M., Rowland, A. A. & Voeltz, G. K. Endoplasmic reticulum-endosome contact increases as endosomes traffic and mature. *Mol. Biol. Cell* **24**, 1030–1040 (2013).
25. Walia, K. et al. SARS-CoV-2 virulence factor ORF3a blocks lysosome function by modulating TBC1D5-dependent Rab7 GTPase cycle. *Nat. Commun.* **15**, 2053 (2024).
26. Tremel, S. et al. Structural basis for VPS34 kinase activation by Rab1 and Rab5 on membranes. *Nat. Commun.* **12**, 1564 (2021).
27. Jongsma, M. L. et al. An ER-associated pathway defines endosomal architecture for controlled cargo transport. *Cell* **166**, 152–166 (2016).
28. Kalaidzidis, I. et al. APPL endosomes are not obligatory endocytic intermediates but act as stable cargo-sorting compartments. *J. Cell Biol.* **211**, 123–144 (2015).
29. Steinberg, F., Heesom, K. J., Bass, M. D. & Cullen, P. J. SNX17 protects integrins from degradation by sorting between lysosomal and recycling pathways. *J. Cell Biol.* **197**, 219–230 (2012).
30. Bakker, J., Spits, M., Neefjes, J. & Berlin, I. The EGFR odyssey - from activation to destruction in space and time. *J. Cell Sci.* **130**, 4087–4096 (2017).
31. Cullen, P. J. & Steinberg, F. To degrade or not to degrade: Mechanisms and significance of endocytic recycling. *Nat. Rev. Mol. Cell Biol.* **19**, 679–696 (2018).
32. McNally, K. E. et al. Retriever is a multiprotein complex for retromer-independent endosomal cargo recycling. *Nat. Cell Biol.* **19**, 1214–1225 (2017).
33. Simonetti, B. & Cullen, P. J. Actin-dependent endosomal receptor recycling. *Curr. Opin. Cell Biol.* **56**, 22–33 (2019).
34. Steinberg, F. et al. A global analysis of SNX27-retromer assembly and cargo specificity reveals a function in glucose and metal ion transport. *Nat. Cell Biol.* **15**, 461–471 (2013).
35. Simonetti, B. et al. SNX27-Retromer directly binds ESCPE-1 to transfer cargo proteins during endosomal recycling. *PLoS Biol.* **20**, e3001601 (2022).
36. Derivery, E. et al. The Arp2/3 activator WASH controls the fission of endosomes through a large multiprotein complex. *Dev. Cell* **17**, 712–723 (2009).
37. Gomez, T. S. & Billadeau, D. D. A FAM21-containing WASH complex regulates retromer-dependent sorting. *Dev. Cell* **17**, 699–711 (2009).
38. Jia, D. et al. WASH and WAVE actin regulators of the Wiskott-Aldrich syndrome protein (WASP) family are controlled by analogous structurally related complexes. *Proc. Natl Acad. Sci. USA* **107**, 10442–10447 (2010).
39. Zech, T. et al. The Arp2/3 activator WASH regulates alpha5beta1-integrin-mediated invasive migration. *J. Cell Sci.* **124**, 3753–3759 (2011).
40. Dostal, V., Humhalova, T., Berankova, P., Pacalt, O. & Libusova, L. SWIP mediates retromer-independent membrane recruitment of the WASH complex. *Traffic* **24**, 216–230 (2023).
41. Harbour, M. E., Breusegem, S. Y. & Seaman, M. N. Recruitment of the endosomal WASH complex is mediated by the extended 'tail' of Fam21 binding to the retromer protein Vps35. *Biochem J.* **442**, 209–220 (2012).
42. Wang, D. et al. Capping protein regulates endosomal trafficking by controlling F-actin density around endocytic vesicles and recruiting RAB5 effectors. *Elife* **10**, https://doi.org/10.7554/eLife.65910 (2021).
43. Edwards, M. et al. Capping protein regulators fine-tune actin assembly dynamics. *Nat. Rev. Mol. Cell Biol.* **15**, 677–689 (2014).
44. Funk, J. et al. A barbed end interference mechanism reveals how capping protein promotes nucleation in branched actin networks. *Nat. Commun.* **12**, 5329 (2021).
45. Gomez, T. S., Gorman, J. A., de Narvajas, A. A., Koenig, A. O. & Billadeau, D. D. Trafficking defects in WASH-knockout fibroblasts originate from collapsed endosomal and lysosomal networks. *Mol. Biol. Cell* **23**, 3215–3228 (2012).
46. Puthenveedu, M. A. et al. Sequence-dependent sorting of recycling proteins by actin-stabilized endosomal microdomains. *Cell* **143**, 761–773 (2010).
47. Jimenez, A. J., Divoux, S., Goud, B. & Perez, F. Phase partitioning rules Rab domain formation, growth and identity. *bioRxiv*, 2023.2004.2017.537227, https://doi.org/10.1101/2023.04.17.537227 (2024).
48. Thankachan, J. M. & Setty, S. R. G. KIF13A-A key regulator of recycling endosome dynamics. *Front Cell Dev. Biol.* **10**, 877532 (2022).
49. Burden, J. J., Sun, X. M., Garcia, A. B. & Soutar, A. K. Sorting motifs in the intracellular domain of the low density lipoprotein receptor interact with a novel domain of sorting nexin-17. *J. Biol. Chem.* **279**, 16237–16245 (2004).
50. Farfan, P. et al. A sorting nexin 17-binding domain within the LRP1 cytoplasmic tail mediates receptor recycling through the basolateral sorting endosome. *Traffic* **14**, 823–838 (2013).
51. Valdmanis, P. N. et al. Mutations in the KIAA0196 gene at the SPG8 locus cause hereditary spastic paraplegia. *Am. J. Hum. Genet* **80**, 152–161 (2007).
52. Bogucki, P. & Sobczynska-Tomaszewska, A. First patient with hereditary spastic paraplegia type 8 in Poland. *Clin. Case Rep.* **5**, 1468–1470 (2017).
53. Jahic, A. et al. A novel strumpellin mutation and potential pitfalls in the molecular diagnosis of hereditary spastic paraplegia type SPG8. *J. Neurol. Sci.* **347**, 372–374 (2014).
54. Clemen, C. S. et al. Strumpellin is a novel valosin-containing protein binding partner linking hereditary spastic paraplegia to protein aggregation diseases. *Brain* **133**, 2920–2941 (2010).
55. Rowland, A. A., Chitwood, P. J., Phillips, M. J. & Voeltz, G. K. ER contact sites define the position and timing of endosome fission. *Cell* **159**, 1027–1041 (2014).
56. Allison, R. et al. Defects in ER-endosome contacts impact lysosome function in hereditary spastic paraplegia. *J. Cell Biol.* **216**, 1337–1355 (2017).
57. Park, S. H., Zhu, P. P., Parker, R. L. & Blackstone, C. Hereditary spastic paraplegia proteins REEP1, spastin, and atlastin-1 coordinate microtubule interactions with the tubular ER network. *J. Clin. Invest* **120**, 1097–1110 (2010).
58. Blackstone, C., O'Kane, C. J. & Reid, E. Hereditary spastic paraplegias: membrane traffic and the motor pathway. *Nat. Rev. Neurosci.* **12**, 31–42 (2011).
59. Rivero-Rios, P. et al. Recruitment of the SNX17-Retriever recycling pathway regulates synaptic function and plasticity. *J. Cell Biol.* **222**, https://doi.org/10.1083/jcb.202207025 (2023).
60. Lauffer, B. E. et al. SNX27 mediates PDZ-directed sorting from endosomes to the plasma membrane. *J. Cell Biol.* **190**, 565–574 (2010).
61. Loo, L. S., Tang, N., Al-Haddawi, M., Dawe, G. S. & Hong, W. A role for sorting nexin 27 in AMPA receptor trafficking. *Nat. Commun.* **5**, 3176 (2014).
62. Hussain, N. K., Diering, G. H., Sole, J., Anggono, V. & Huganir, R. L. Sorting Nexin 27 regulates basal and activity-dependent trafficking of AMPARs. *Proc. Natl Acad. Sci. USA* **111**, 11840–11845 (2014).
63. Temkin, P. et al. The retromer supports AMPA receptor trafficking during LTP. *Neuron* **94**, 74–82 e75 (2017).
64. Halff, E. F., Szulc, B. R., Lesept, F. & Kittler, J. T. SNX27-mediated recycling of neuroligin-2 regulates inhibitory signaling. *Cell Rep.* **29**, 2599–2607 e2596 (2019).
65. Sharma, A. et al. Methods for binding analysis of small GTP-binding proteins with their effectors. *Methods Cell Biol.* **166**, 235–250 (2021).

66. Ezratty, E. J., Partridge, M. A. & Gundersen, G. G. Microtubule-induced focal adhesion disassembly is mediated by dynamin and focal adhesion kinase. *Nat. Cell Biol.* **7**, 581–590 (2005).
67. Williamson, C. D., Guardia, C. M., De Pace, R., Bonifacino, J. S. & Saric, A. Measurement of lysosome positioning by shell analysis and line scan. *Methods Mol. Biol.* **2473**, 285–306 (2022).
68. Bhatia, T., Cornelius, F. & Ipsen, J. H. Capturing suboptical dynamic structures in lipid bilayer patches formed from free-standing giant unilamellar vesicles. *Nat. Protoc.* **12**, 1563–1575 (2017).
69. Barthel, L. K. & Raymond, P. A. In situ hybridization studies of retinal neurons. *Methods Enzymol.* **316**, 579–590 (2000).

## Acknowledgements

S.P. and K.W. acknowledge fellowship support from IISER Mohali and the Council of Scientific & Industrial Research (CSIR), respectively. R.P. acknowledges salary support from the SERB-POWER Grant [SPG/2021/002790]. P.S. and K.K.B. acknowledge post-doctoral fellowship support from DBT [DBT-RA/20123/July/N/4351] and IISER Mohali, respectively. This research was supported by the Department of Biotechnology (DBT)/Wellcome Trust India Alliance Senior Fellowship [IA/S/19/1/504270], DBT grant [BT/PR53883/BMS/85/123/2024], SERB-POWER Grant [SPG/2021/002790], award for exploratory research on rare genetic disorders from Google (Asia Pacific Pte. Ltd.) and intramural funding from IISER Mohali to M.S. This work was supported by grants from ANRF [CRG/2022/003266] and CSIR [HCP532401] to A.T. This work was supported by grants from DBT [BT/PR36570/BRB/10/1976/2021 and BT/PR53768/BMS/85/157/2024] to R.R., and DBT Ramalingaswami grant [BT/RLF/Re-entry/06/2020] and [IC-12025(22)/1/2023-ICD-DBT] to T.B. The authors acknowledge the Department of Science & Technology [FIST; SR/FST/LS-II/2017/97] for access to the super-resolution confocal microscope used in some of the imaging experiments. The funders had no role in the study design, data collection, interpretation, or decision to submit the manuscript for publication. The authors acknowledge all colleagues who shared the plasmids used in this study. The authors would also like to acknowledge Prateek Arora and Rahul Kirti (IISER Mohali FACS Facility) for their technical assistance with flow cytometry-related experiments, as well as all lab members of M.S. and A.T. for their helpful discussions.

## Author contributions

S.P. designed and performed the majority of the experiments, analyzed the results, and prepared the figures. M.S. and A.T. conceived and designed the study and wrote the manuscript. R.P., K.W., and A.A. performed some of the protein-protein interaction assays and assisted in other experiments. P.S., S.P., and R.R. designed, performed, and analyzed the zebrafish experiments. K.K.B., R.G., and Y.V. contributed to the generation of molecular biology reagents and assisted in the yeast-two-hybrid assays. S.G. and T.B. prepared the GUVs and performed the GUV experiments.

## Competing interests

The authors declare no competing interests.

## Additional information

**Supplementary information** The online version contains supplementary material available at https://doi.org/10.1038/s41467-025-65568-4.

**Correspondence** and requests for materials should be addressed to Mahak Sharma.

**Peer review information** *Nature Communications* thanks Anbing Shi and the other, anonymous, reviewer(s) for their contribution to the peer review of this work. A peer review file is available.

**Reprints and permissions information** is available at http://www.nature.com/reprints